land

MDPI

Review

The Shadow Effect on Surface Biophysical Variables Derived from Remote Sensing: A Review

Seyed Kazem Alavipanah [1,*], Mohammad Karimi Firozjaei [1], Amir Sedighi [1], Solmaz Fathololoumi [2], Saeid Zare Naghadehi [3], Samiraalsadat Saleh [4], Maryam Naghdizadegan [1], Zinat Gomeh [1], Jamal Jokar Arsanjani [5], Mohsen Makki [6], Salman Qureshi [6], Qihao Weng [7], Dagmar Haase [6], Biswajeet Pradhan [8], Asim Biswas [2] and Peter M. Atkinson [9]

1 Department of Remote Sensing and GIS, Faculty of Geography, University of Tehran, Tehran 14178-53933, Iran
2 School of Environmental Sciences, University of Guelph, Guelph, ON N1G 2W1, Canada
3 Department of Civil, Environmental and Geomatics Engineering, College of Engineering and Computer Science, Florida Atlantic University, 777 Glades Road, Boca Raton, FL 33431, USA
4 Department of Geography and Environmental Science, North Texas University, Denton, TX 76203, USA
5 Geoinformatics Research Group, Department of Planning and Development, Aalborg University Copenhagen, A.C. Meyers Vænge 15, DK-2450 Copenhagen, Denmark
6 Department of Geography, Humboldt University Berlin, Unter den Linden 6, 10099 Berlin, Germany
7 Department of Land Surveying and Geo-Informatics, Hong Kong Polytechnic University, 11 Yuk Choi Road Hung Hom, Kowloon, Hong Kong, China
8 Center for Advanced Modeling and Geospatial Information Systema (CAMGIS), School of Civil and Environmental Engineering, Faculty of Engineering and IT, University of Technology Sydney, CB11.06.106, Building 11, 81 Broadway, Ultimo, NSW 2007, Australia
9 Lancaster Environment Center, Faculty of Science and Technology, Lancaster University, Bailrigg, Lancaster LA1 4YR, UK
* Correspondence: salavipa@ut.ac.ir; Tel.: +98-21-6111-3536

Abstract: In remote sensing (RS), shadows play an important role, commonly affecting the quality of data recorded by remote sensors. It is, therefore, of the utmost importance to detect and model the shadow effect in RS data as well as the information that is obtained from them, particularly when the data are to be used in further environmental studies. Shadows can generally be categorized into four types based on their sources: cloud shadows, topographic shadows, urban shadows, and a combination of these. The main objective of this study was to review the recent literature on the shadow effect in remote sensing. A systematic literature review was employed to evaluate studies published since 1975. Various studies demonstrated that shadows influence significantly the estimation of various properties by remote sensing. These properties include vegetation, impervious surfaces, water, snow, albedo, soil moisture, evapotranspiration, and land surface temperature. It should be noted that shadows also affect the outputs of remote sensing processes such as spectral indices, urban heat islands, and land use/cover maps. The effect of shadows on the extracted information is a function of the sensor–target–solar geometry, overpass time, and the spatial resolution of the satellite sensor imagery. Meanwhile, modeling the effect of shadow and applying appropriate strategies to reduce its impacts on various environmental and surface biophysical variables is associated with many challenges. However, some studies have made use of shadows and extracted valuable information from them. An overview of the proposed methods for identifying and removing the shadow effect is presented.

Keywords: shadow; surface biophysical variables; shadow detection; de-shadowing; remote sensing

Citation: Alavipanah, S.K.; Karimi Firozjaei, M.; Sedighi, A.; Fathololoumi, S.; Zare Naghadehi, S.; Saleh, S.; Naghdizadegan, M.; Gomeh, Z.; Arsanjani, J.J.; Makki, M.; et al. The Shadow Effect on Surface Biophysical Variables Derived from Remote Sensing: A Review. *Land* **2022**, *11*, 2025. https://doi.org/10.3390/land11112025

Academic Editor: Dailiang Peng

Received: 15 October 2022
Accepted: 10 November 2022
Published: 12 November 2022

1. Introduction

Extraction of information from satellite sensor images can be challenging due to effects on the recorded signal of natural phenomena that are not the subject of interest, such as from the atmosphere, soil, and water. Additionally, the limited spatial, spectral, temporal and

radiometric resolutions of satellite sensors must be considered as serious challenges [1,2]. These challenges can cause geometric, atmospheric, and topographic errors in feature extraction [3,4], which reduce the quality of the extracted information. An issue that is common, but relatively unstudied, is the effect of shadow on the recorded signal [5–7]. For example, the micro-scale shadow distribution within each pixel is a key parameter affecting directly spectral reflectance anisotropy [8].

Shadow is created via the interaction of solar light with the canopy over various types of terrain cover. Shadows are dark and their properties, shape, and form depend on several parameters including Sun–target–sensor geometry, atmospheric scattering, illumination intensity, and canopy type [9]. The effects of shadow vary according to the time of satellite sensor image acquisition (hour, day, and season) [10], as shadow coverage and intensity vary with the time of day [9]. Shadow shape is also influenced by topography [11,12]. High elevation relief can cause relief shadows, and topographic complexity can cause canopy mutual shadowing [13]. This can mix spectral features of objects, mainly in fine spatial resolution images [7,14].

Four main groups of shadows have been recognized: shadows from (1) urban phenomena, (2) topography, (3) clouds, or (4) a combination of these [15]. Many studies reported that shadow areas in satellite sensor imagery can be used to obtain useful information such as thermal inertia, emissivity, soil moisture (SM), forest structural characteristics, geological feature characteristics, object height measurement, and ecological and urban studies [16–18].

Shadow has more often been considered as noise in passive satellite sensor images [19–21] because shadow causes a change in the spectral response of objects at the thermal and optical wavelengths of the electromagnetic spectrum. Therefore, shadow can affect the interpretation of phenomena on Earth. Moreover, shadow can have major effects on satellite-derived surface biophysical characteristics [22]. Simpson, et al. [23] outlined that shadows can produce low and negative values in the normalized difference vegetation index (NDVI) especially in dense vegetation regions. Based on [24], shadow is an error source in detection of snowy or glacier areas in mountainous regions using satellite sensor images. Beside optical bands, thermal bands are also used in mountainous regions to minimize the negative effects of shadow. Shadow causes bias in land use/cover (LULC) mapping in areas with severe topography and in urban areas [25,26]. Assessment and enhancement of LULC change, feature extraction, and image mosaicking are all affected by shadow [27,28]. Negative effects of shadow on indices and models in thermal and optical RS such as impervious surfaces [29,30], vegetation [31], land surface temperature (LST) [32–34], SM [35], water [36], evapotranspiration [37,38], LULC [39,40], snow [24,41], and albedo [42,43] were also emphasized.

Despite the above, shadows provide useful information in some cases. The structural characteristics of forests can be modeled using tree shadows and their canopies in fine spatial resolution images such as Quickbird [44]. Shadow can also be useful for assessing geological features, especially while the Sun's altitude is low, since shadows can describe the smallest elevation changes in an area [45]. A shadow's size, shape, and form, along with its location, provide information not only about the attributes of a natural feature or object, but also about the position, height, and direction of that feature or object in both natural and urban environments [44,46–49].

Based on the aforementioned details, shadow detection and compensation, and the correction of spectral features in shaded areas are essential. In coarse spatial resolution images, shaded surfaces are usually combined with sunlit surfaces, whereas in fine spatial resolution images, shadows are more problematic. Therefore, the detection, correction and removal of shadows is an even greater challenge for unmanned aerial vehicle (UAV) images which generally have a much finer spatial resolution [9].

Various methods have been presented for shadow detection, and their discrimination from areas without shadow, using satellite sensor images. The choice of method for shadow detection affects the accuracy of results. Most studies are focused on recovering information

or minimizing shadow effects in satellite sensor images, because valuable information exists in shadow areas [50]. Moreover, information in adjacent areas can be used for shadow areas [51]. Shadow correction methods can be divided broadly into four categories according to the origin of the shadow: topographic shadow correction, urban shadow correction, cloud shadow correction, and composite shadow correction [6,15]. Typically, the resolution of the sensor affects the de-shadowing procedure applied to satellite sensor images. The common topographic de-shadowing methods are: multisource classification and Digital Elevation Models (DEMs)-based and band ratio [15,52]. Urban shadow is more difficult to remove than other shadows [53,54]. In previous studies, techniques such as Gamma correction [55], object-based approach [28,56,57], invariant color model [58], and machine learning methods [59–61] have been used to correct, or reduce, the effect of shadow. Clouds and their shadows affect the spectral characteristics of features in optical and thermal RS [62,63] and, hence, reduce the quality of RS data. In previous studies, different models including semi-physical fusion approach [64], robust nonlinear wavelet regression [65], and wavelet image fusion were applied for correction of shadow effects in satellite sensor images [66].

In recent years, a few critical review articles such as Shahtahmassebi, et al. [15] and Mostafa [67] have presented several methods of shadow detection and compensation in satellite sensor imagery. Shadow correction algorithms are the main subject of these review articles. Considering the direct and indirect effects of shadow on information extraction from satellite sensor images, studying the algorithms for shadow detection and their potential for restoring information in both the optical and thermal bands of satellite sensor images is of significant importance. Hence, this review considers the effects of shadows on RS-driven surface biophysical variables and outputs of RS processes. Moreover, the types of both shadow detection and de-shadowing methods are reviewed. The main contribution of this review is the exploration of shadow effects on optical and thermal indices of surface biophysical variables.

2. Materials and Methods

This review employed a systematic approach to search for the most relevant papers and select papers based on a rigorous set of evaluation criteria. The selected papers were classified and investigated based on the study objectives. The systematic review was conducted in three systematic steps to achieve the study objectives. In this study, the methods introduced and developed by [68,69] were used.

2.1. Papers Search

In the first step, to identify the papers that met our criteria set, the search focused on the effect of shadow on surface biophysical variables derived from RS. To perform this, scientific and academic electronic databases such as Scopus, Science Direct, Web of Science, and Google Scholar were searched. Searches were conducted from the date of publication of the first relevant paper until December 2021 in these databases. To find the most relevant papers, the following keywords were used: “shadow”, “effect of shadow”, “cloud shadows”, “shadows from topography”, “shadows from urban structures”, “combined shadows”, “effect of shadow on environmental variables”, “effect of shadow on surface biophysical variables”, “effect of shadow on vegetation index”, “effect of shadow on impervious surface cover”, “effect of shadow on LST”, “effect of shadow on the vegetation index”, “effect of shadow on water and water stress indices”, “effect of shadow on snow mapping”, “effect of shadow on albedo”, “effect of shadow on soil moisture”, “effect of shadow on evapotranspiration”, “effect of shadow on urban heat island(s)”, and “effect of shadow on LULC classification”. The initial search found 2555 papers within 1975 to 2021 using the search keywords. That is, these papers contained at least one of the keywords.

2.2. Selection of Papers

In the second step, peer reviewed articles and conference papers that dealt with the effect of shadow on surface biophysical variables derived from RS were selected, excluding book chapters and conference abstracts. To eliminate irrelevant papers, several criteria were applied. For example, redundant papers (n = 420) found in different databases were eliminated. Non-English papers (n = 180) were excluded. Finally, 1955 papers of the 2555 papers were selected for this review (Figure 1).

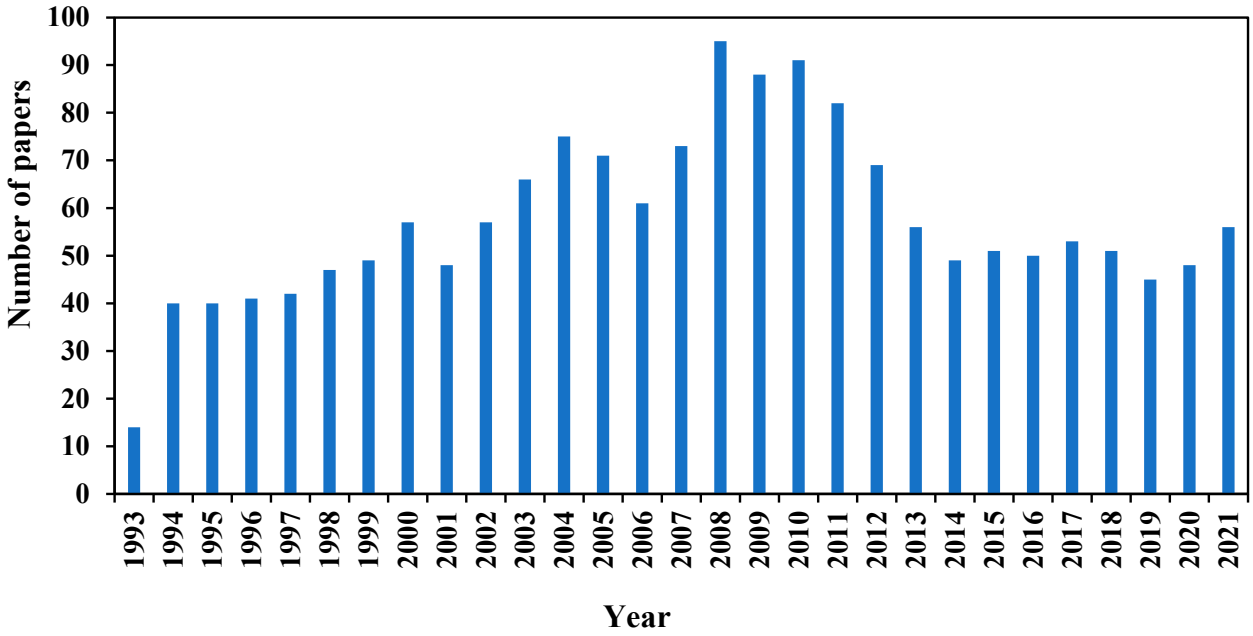

Figure 1. The number of papers selected for this review based on the selection criteria plotted against year.

The following details were collected into a database as part of the evaluation process for the selected papers: main objective of the paper, authors, country of affiliation, year of publication, scope, and name of the journal, spatial resolution of utilized data, shadow type, methodology and methods, assessment of results, and relevance of the paper with respect to our study objectives.

2.3. Information Extraction and Integration

The assembled database was used to extract important information about the effect of shadow on various surface biophysical variables such as albedo, evapotranspiration, impervious surface cover (ISC), SM, LST, and urban heat islands (UHIs), spectral indices such as vegetation, water and snow covers, and LULC classification, separately. These variables are among the most relevant and common variables that can be extracted from remote sensing data, which are important in various environmental applications. Therefore, studying the effect of shadow on these variables is of great importance. Afterwards, the redundant information was integrated and described in a specific section related to a specific parameter. Additionally, valuable information was extracted from the assembled papers about shadow detection and de-shadowing methods. At the end of this paper, a comprehensive overview of different methods for identifying and removing shadow is presented.

The de-shadowing methods developed in previous studies are different for urban, cloud and topographic shadows. Therefore, in this study, de-shadowing methods are presented separately for each shadow type. Hence, the information from 'shadow type' and 'year of publication' was used to analyze the annual growth and temporal distribution of papers (Figure 2). This analysis grouped the papers to help support the main objective of the study.

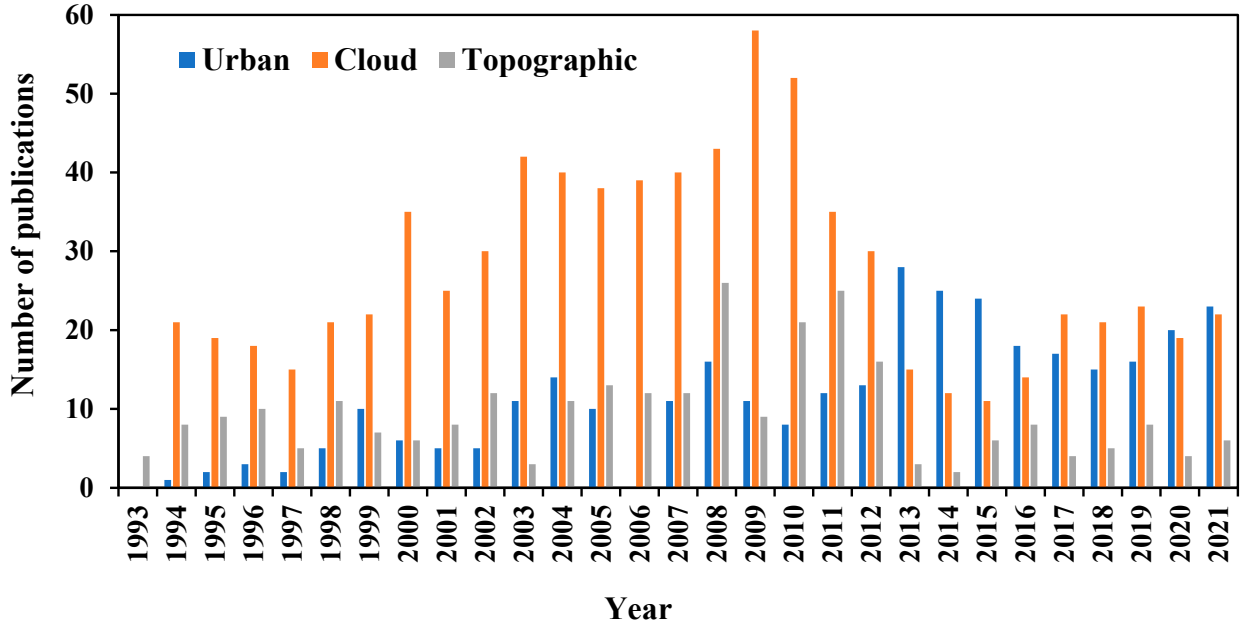

Figure 2. Plot of publications in the three different categories "shadow type" against time.

3. Results

3.1. Effect of Shadow on RS-Driven Variables and Outputs

The shadow problem is obvious in fine, moderate, and coarse spatial resolution images, and in the extraction of biophysical variables [70]. In a satellite sensor image, some areas may be shaded by clouds, mountains, hills, trees, and urban objects. A decrease in radiance in the shaded target is the main negative effect of shadow. It may also affect biophysical variables, including albedo, evapotranspiration, impervious surface cover (ISC), SM, LST, and urban heat islands (UHIs), spectral indices (vegetation, water, and snow), and LULC classification. These are discussed, in turn, below.

3.1.1. Albedo

Albedo depends on the atmosphere and land surface properties. Surface topography causes changes in solar illumination geometry and land surface properties derived from RS data [71]. Therefore, the effects of shadow on albedo over a rough surface are linked to the properties' variation in the subpixel topography, azimuth, and zenith angles [72–74].

Overall, the Lambertian assumption ignores canopy structure and shadows that impact adjacent areas, which significantly affect the values of albedo. Due to these geometric optical effects, surfaces appear brighter when the source of light is behind the sensor (backscattering) or darker when the source of light is in opposition to the viewing angle of the sensor (forward scattering). This significantly affects the retrieval of surface albedo. As a result of the shadow effect of skyscraper buildings, Lee, et al. [75] found that densely built-up areas have an estimated albedo that is 17% lower than other areas.

Albedo becomes more sensitive to aspect as slope increases. Furthermore, diffused radiation and terrain shadowing from adjacent surfaces significantly affect the albedo values [76]. Shadows due to neighboring topography significantly affect the black-sky albedo. However, the white-sky albedo is independent of shadow and solar illumination geometry effects [71]. Topographic impacts on albedo over rough surfaces are commonly attributed to the integrated effects of subpixel slopes and aspects within each pixel of an image [73,77]. Neglecting the topography, spatial variation within pixels in albedo calculations on a rough surface can lead to remarkable error [72–74], for example, 33% relative error in albedo estimation for a slope average of 40° [73]. Cherubini, et al. [42] showed that albedo estimation is also extremely sensitive to topography of subpixels in

MODerate resolution Imaging Spectroradiometer (MODIS) images, and the albedo on a rough surface can change up to 100% for vegetation in a pixel of MODIS imagery.

3.1.2. Evapotranspiration

Evapotranspiration includes lost water from both plants and soil. Exact modeling of evapotranspiration is helpful in many agricultural, ecological, water management, and environmental applications [37,38,78]. There are, however, some challenges associated with assessing vegetation-shading effects on estimating evapotranspiration, as the shadow zone is usually difficult to measure and changes with the solar zenith angle throughout the day and with the growth of the plant.

It is important for vegetation restoration to consider the water budget of semi-arid regions, which is dominated by evaporation from the soil and transpiration from plants. In sparsely vegetated areas, shadows cast by sparse vegetation reduce incoming solar radiation, which can affect the biotic processes of plants and the transportation of land-atmosphere flux. As a result of vegetation structure intercepting solar radiation and the shadows cast by it, the LST varies spatially in shadow-free and shadow-affected areas, resulting in spatial variation in evapotranspiration. Many traditional methods acknowledge that the shadow reduces near-ground radiation. However, few estimate the direct impact of shadows on LST, which is vital for calculating evapotranspiration, particularly in RS because LST incorporates the effects of changes in ambient temperature, wind dynamics, soil thermal conductivity, and soil moisture content induced by climate change [37].

3.1.3. Impervious Surface Cover (ISC)

Knowledge of the distribution, pattern, and geometry of ISC is important for a wide range of topics in urban planning, ecological process modeling, environmental modeling, and resource management globally, regionally, and locally [79–84]. However, shadows due to mountains, trees, clouds, or tall buildings in satellite sensor images can dramatically affect the accuracy of mapping ISC [70,85–87].

Mixing of ISC class with sand, soil, and shadow effects during the ISC prediction process was reported as a major problem [85,88]. Shadows of trees and buildings have a major influence on ISC prediction. Some shadows from buildings are mixed together, and some roads are covered by trees or their shadows. The impact of building shadows on ISC extraction is greater than for tree shadows. In fine spatial resolution images of urban environments (i.e., the greatest source of ISC), shadows are generally induced by low Sun elevation and tall buildings [29,30].

The spectral similarity between shaded ISC, shadows in other areas and water bodies is a major challenge in mapping ISC automatically using fine and medium resolution images in the urban environment [46,79,87]. In Figure 3a, for the Landsat Thematic Mapper (TM) sensor, the spectra of ISC with low albedo are very similar to those of vegetation shadows. Therefore, TM images cannot be used to readily distinguish these two surfaces from each other. For Hyperion (Figure 3b), the spectra of vegetation shadow and ISC with low albedo are sufficiently separated [89].

Some studies have tried to eliminate the effects of shadows by using thermal bands in built-up indices such as the Enhanced Built-up and Bareness Index (EBBI) and Normalized Difference Bareness Index (NDBaI) for built-up area mapping, because thermal bands can detect albedo levels in built-up areas [90–92]. Moreover, the normalized difference impervious index (NDII), which was developed based on thermal infrared and red bands, is frequently used to extract ISC areas. Due to the fact that the shadows cast by vegetation and mountains are generally cooler than those cast by tall buildings, the ISC extracted by NDII was found to be not affected by shadows [93]. Another index in this domain is the normalized difference impervious surfaces index (NDISI), which can remove shadow noise and greatly reduce the background effects of sand and soil [94].

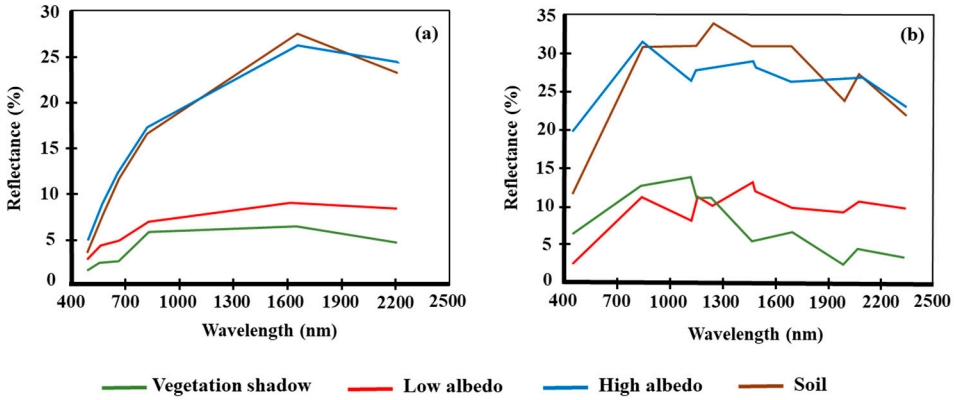

Figure 3. Spectra of the main features: (**a**) spectra acquired by TM sensor, and (**b**) spectra acquired by Hyperion sensor (adapted from [89]).

In [86], linear spectral unmixing was applied in shadowed and non-shadowed regions. Spectral characteristics of urban objects in shadowed regions differ greatly from those in non-shadowed regions [86]. Moreover, a hierarchical classification strategy was used for ISC extraction in shadowed and non-shadowed regions to overcome the shadow issue in fine resolution images [95,96].

Object-Based Image Analysis (OBIA) is more efficient than conventional pixel-based approaches for extracting ISC at fine resolution [70] because OBIA is able to deal with spectral variability within classes [3,29,30]. Meanwhile, this model uses object-oriented segmentation and establishes a multi-scale model, topology, and textures to establish a hierarchical network. This model is efficient in dealing with the shadow in urban environments [29,30].

3.1.4. Soil Moisture (SM)

SM is a key factor in land, atmosphere, and climate systems [97]. At different scales, it impacts the water, energy, biophysical, and biogeochemical cycles [98,99]. In some studies, the vegetation coverage shadow was found to affect spatial variation in SM. Hence, SM was obtained based on the LST differences between sunlit surfaces and shadows. Useful information on SM can be obtained from the LST difference between shadow and sunlit areas [35].

Based on the thermal equilibrium equations, the comparison of shadow LST with adjacent areas under direct sunlight contains valuable information. Practically, this is because shadow areas receive only the sky components of radiation. Conversely, sunlit areas receive direct radiation from the Sun in addition to the sky components, which causes a difference in LST between them. This LST difference can be used as the basis for SM calculation. The results indicated that a method based on shadow and sunlit areas was able to estimate SM [35].

SM is commonly calculated based on a linear function between SM and thermal inertia for different types of soil [100]. Therefore, in this method, the challenge is to prepare two images with maximum thermal difference due to a change in environmental conditions when the images were acquired: according to the thermal equilibrium equations, temperature differences between shadow regions, and adjacent areas in direct sunlight provide valuable information for calculating thermal inertia and SM [35].

3.1.5. LST and Urban Heat Islands (UHIs)

LST shows the amount of emitted radiation from the surface and subsurface and dictates the exchange of energy between the Earth's surface and atmosphere. Satellite-derived LST is of paramount importance in various applications including energy balance [101–104], environmental monitoring [105], geological structure [106], climate change

and urban studies [107–111], evapotranspiration surface moisture, and water resources management [112–115].

Satellite-derived LST is a directional variable [32–34,116] because different viewing and illumination angles create different shadows. Different viewing and illumination angles would likely result in different LST values for LST estimations for the same scene and the same sensor. These values would depend on variables such as Sun aspect, surface cover, and soil properties. The LST is also greatly affected by surface structure due to shadowing effects and dependence on azimuth and zenith view angles. However, these effects are usually overlooked in many studies. When evaluating the accuracy of LST estimations through comparisons with ground observations, or comparing LST products, viewing angles and illumination geometries need to be considered [32,33,117]. The results of the study by Ermida, et al. [117] indicated that the differences between LST derived from Spinning Enhanced Visible and Infrared Imagers (SEVIRI) and MODIS sensors during daytime were significant due to shadowing effects. Recently, the influence of shadows on the calculation of LST from UAV images with fine spatial resolution before and after shadow correction was evaluated. It was found that shadow correction is necessary to retrieve vegetation and LST [118].

A model for estimating the impact of surface structure on LST was developed by Ermida, et al. [119]. This model was used to calculate the temperature composite in the field of view (FOV) of the SEVIRI and MODIS sensors. As a result, the bias in daytime LST values derived from SEVIRI and MODIS was reduced by 1 to 2.5 °C compared with a simpler method. A significant decrease in LST differences between MODIS and SEVIRI was also observed when the effects of viewing geometry were corrected. The variations in shadow, sunlit area, canopy, and near-surface air temperatures during a diurnal cycle are illustrated in Figure 4. There is no direct incoming solar radiation in shaded areas, so temperatures there are generally considered to be similar to near-surface air or tree canopy temperatures [119]. Based on a similar study, the difference in soil surface temperature between shaded and sunlit areas was found to be approximately 10 °C [120].

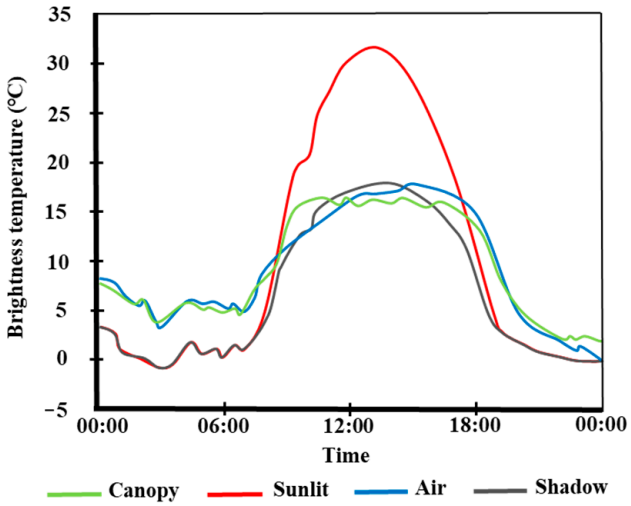

Figure 4. Shadow, sunlit area, canopy, and near-surface air temperatures during a diurnal cycle (adapted from [119]).

On the other hand, surface topography and roughness can have major effects on the LST. Some topography effects are surface shadow, contribution of surrounding surface radiation, aspect angles, and slope that change solar radiative heating. These effects cause a large discrepancy between directional brightness temperature (BT) and equivalent BT [121,122]. Surface roughness leads to shadows and scattering of surface-emitted radiation flux on surrounding surfaces [122].

The relationship between the shaded surface fraction and LST in urban areas was studied by Kato, et al. [123]. Figure 5 shows the relationship between shaded surface

fraction and LST in different surface covers in different seasons. LST is more affected by vegetation types than the area of vegetation, so there is no clear relationship between LST and the vegetation fraction. Furthermore, water body fraction is not clearly correlated with LST. However, shaded areas influence LST. In areas with larger values of shaded fraction, the deviation of LST caused by surface cover in sunlit areas was smaller.

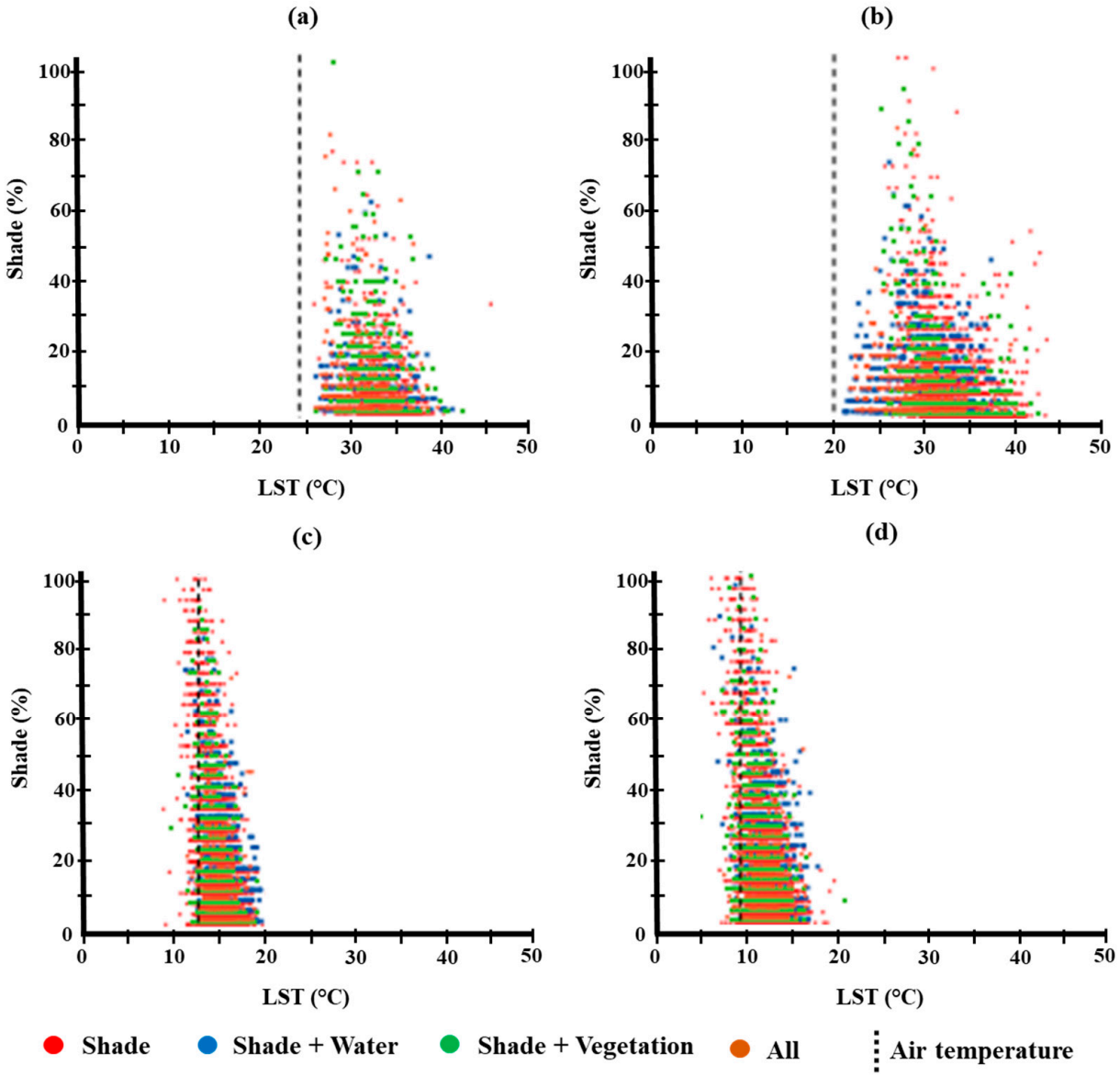

Figure 5. Scatterplots between shaded fraction and LST for (**a**) 16 September 2004, (**b**) 30 April 2009, (**c**) 14 December 2007, and (**d**) 17 January 2009 (adapted from [123]).

As shown in Figure 5, the scatterplots show a triangle shape characteristic of smaller LST ranges with larger values of the shaded fraction. Based on these results, LST differences largely depend on the thermal properties and evapotranspiration of sunlit areas. Despite shaded fraction values, the smallest value of LST in shaded areas is smaller than the air temperature in winter. Conversely, the smallest value of LST is larger than the air temperature in spring and autumn. Accordingly, air temperature cannot be substituted for LST in shaded areas.

The major reason for UHI intensification in cities is more radiation absorption by ISC, because the vegetation density and the overall level of shadow are reduced [16,124,125]. Tall buildings and trees often cast shadows in urban areas. Their distribution indicates intensive seasonal changes that significantly affect UHI [124]. Both the cooling and shadow

effects of vegetation cover affect LST [126]. Some previous studies reported that the shadows of buildings reduce the incoming solar radiance in summer [16,124]. Urban thermal environments have been significantly influenced by building shadows, that is, by preventing solar radiation from penetrating into the urban areas [127].

The LST of ISC pixels is more responsive to building shadows than vegetation pixels, since vegetation's self-regulation mechanism reduces the cooling effect of building shadows. LST distribution is strongly affected by building shadows in winter. Despite the previous studies, extensive analysis must be employed to determine the influence of building shadows on seasonal variation in the UHI in urban areas [128]. Yu, et al. [128] concluded that the cooling effects of building shadows must be considered to design suitable urban forms to reduce the intensity of UHIs. This result was also suggested by Zhao, et al. [129], who suggested that high buildings can mitigate UHI during the daytime.

3.1.6. Vegetation Indices

Vegetation indices (VIs) are of substantial utility in numerous environmental applications, so the recognition and study of factors affecting VIs is important. A canopy's total reflectance is largely influenced by shadows on its surfaces [130]. Some uncertainties may occur in calculating vegetation variables using VIs, if shadow effects are ignored [131]. Thus, the shadow problem has been highlighted following the growth of different remote sensing data. Several studies have examined the shadow effect on vegetation indices in hyperspectral images [132,133]. As an example, Huemmrich [133] used hyperspectral data to determine the Fraction of Absorbed Photosynthetically Active Radiation (FAPAR) by considering the shadow effect on the Soil Adjusted Vegetation Index (SAVI) and NDVI. Using hyperspectral data, Figure 6 illustrates the spectra from sunlit and shaded leaves [31].

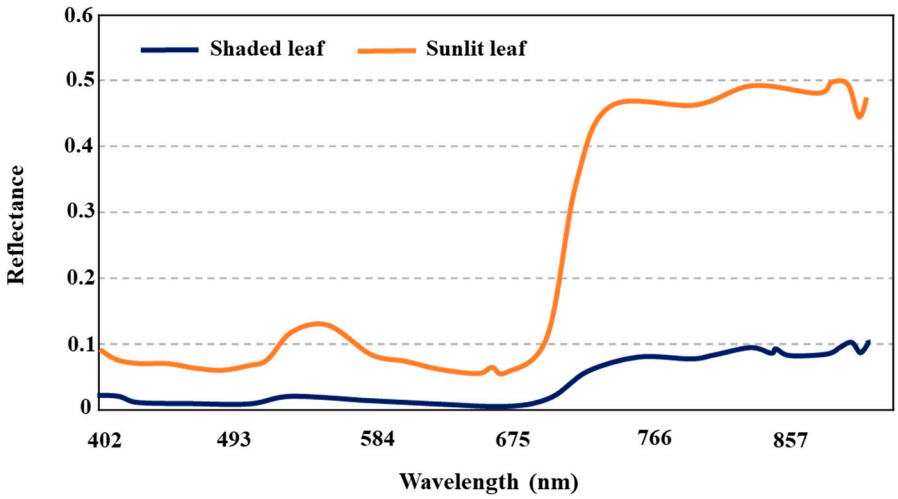

Figure 6. Sunlit and shadowed leaf spectra in the range 400–1000 nm (adapted from [31]).

The reflectance of sunlit leaves is much higher than for shaded leaves at all wavelengths. At visible wavelengths (400–700 nm), shaded leaves do not reflect much except at green wavelengths (540 nm). The reflectance of sunlit leaves was found to be five times more than for shadowed leaves at near-infrared wavelengths. In contrast to the shadowed leaves, the spectra of the sunlit leaves differed in both reflectance and shape, which may affect the calculation of VIs.

NDVI is a key factor in the estimation of land surface emissivity (LSE) and LST, among others [134]. Hence, correction of the shadow effect on NDVI for heterogeneous regions is necessary. Some studies indicated that NDVI is not a suitable quantitative index in sparse vegetation regions because of shadow effects on the surface (Figure 7) [1,135,136].

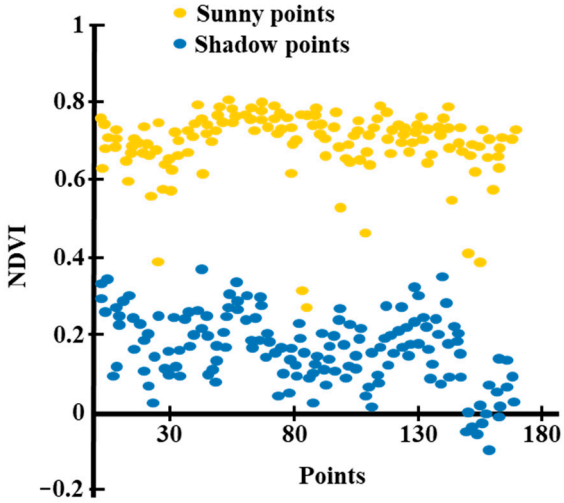

Figure 7. Values of NDVI in shadowed and sunny regions (adapted from [134]).

The effect of shadow on different VIs was investigated by Zhang, et al. [31]. Figure 8 shows the means for various VIs taken from sunlit and shaded areas.

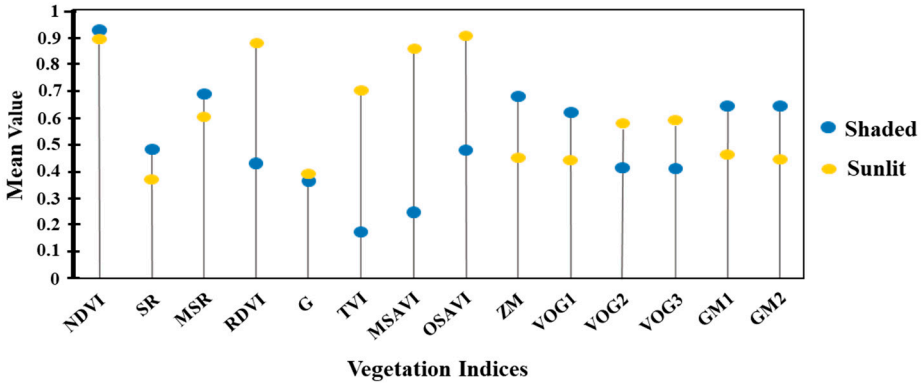

Figure 8. Means of vegetation indices in shaded and sunlit areas [31].

The Modified Soil-Adjusted Vegetation Index (MSAVI) was the most affected by shadows, followed by the Triangular Vegetation Index (TVI). The Greenness (G) and NDVI indices differed slightly between shadowed and sunlit leaves. There was a significant difference in the level of darkness between shadowed vegetation and sunlit vegetation, except for the G and NDVI indices. Shadows significantly affected the MSAVI, TVI, and Ratio Difference Vegetation Index (RDVI) indices, with smaller values in shaded areas. The values of the Simple Ratio (SR) and NDVI indices were both larger in shaded areas [31].

Another shadow effect on vegetation studies is the influence on vegetation water stress detection. In past studies, the performance of PRI and TCARI/OSAVI for vegetation water stress detection was demonstrated in regions including low-albedo surfaces and shadows [137,138]. Thus, some studies have documented certain problems with these indices, such as shadow/sunlit fraction, viewing angles, and illumination geometry effects.

3.1.7. Water Indices

Remote sensing data are commonly applied to mapping water bodies and water resources management [139–142]. Broadly, water surface extraction methods fail to separate water surfaces from mountain shadows and low-albedo surfaces in natural environments as well as shadows of buildings and clouds in urban areas [143]. For satellite sensor images, it is generally challenging to separate shadows from water, especially in urban areas [36].

Several methods were employed to extract water surface information from satellite sensor imagery [144,145], depending on the number of bands. Water indices are usually

calculated using two bands from a multispectral image [146]. In these methods, a threshold is determined for the index to separate water from other surfaces. As a result of threshold value selection, estimated water surface information is often mixed with shadow information [143]. The Modification of Normalized Difference Water Index (MNDWI) can reduce the effect of shadow through simple procedures, but it is difficult to remove.

The shadow effect was considered in recent studies to develop water extraction indices. Xie, et al. [147] introduced a newly developed the Hyperspectral Difference Water Index (HDWI) for extracting water surfaces in regions with shadows over water and low albedo surfaces. A significant source of misclassification in urban areas is shadows cast by tall buildings, which can be reduced through the HDWI. In comparison with other water indices, the HDWI has a high accuracy in identifying shadow pixels that are in the water class and those that are not [147]. In addition, Feyisa, et al. [145] developed an automated water extraction index (AWEI) to increase accuracy in shadow and dark areas on Landsat TM. AWEIsh was introduced for areas that include shadows [145]. They concluded that for narrow water extraction, MNDWI has problems due to cloud and its shadow, while AEWI ameliorates these to some extent [145]. Similarly, another study reported that the Modified Optimization Water Index (MOWI) performs more accurately in different conditions, such as under cloudy conditions, in cloud shadows, and in mountain shadows [148].

3.1.8. Snow Indices

Snow surface mapping and monitoring using snow indices in mountainous regions is an issue because at visible and near-infrared wavelengths, mountain shadows have similar cloud and snow spectra [24,41]. Numerous reflectance and ratio-based methods have tried to distinguish snow from other surface covers, but mountain shadows cause them to fail. The Normalized Difference Snow Index (NDSI) has an advantage in contrast with previous methods because it can detect snow cover under mountain shadows. Based on field observations, the reflectance values and NDSI were determined for different types of surfaces by Kulkarni, et al. [41], as shown in Figure 9.

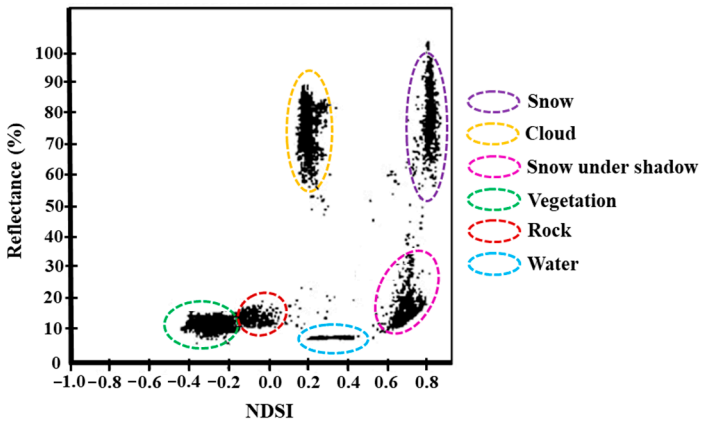

Figure 9. Scatterplot of the reflectance and NDSI values of different surfaces in the Beas basin (date: 17 December 2003) (adapted from [41]).

The results revealed a large difference in snow surface estimation between NDSI and the supervised classification. Snow pixels under mountain shadow were not detectable by supervised classifiers. Surfaces with snow have unique NDSI values, independent of illumination. In other words, the NDSI can distinguish snow and non-snow pixels even under different orientation and slope conditions or under mountain shadow [41].

Thermal bands were used in addition to reflective bands to minimize the negative effects of shadow and topography in mountainous areas. This was performed by Kour, et al. [24] and the performance of different indices for extracting snow surfaces was compared. The results indicated that indices that utilize thermal bands in addition to reflective bands have greater efficiency.

3.1.9. LULC Classification

LULC classification and object detection become problematic because of the shadowing effect of natural phenomena [149,150]. Therefore, shadows are an important factor affecting classification accuracy [27,28], especially in fine resolution images [9]. Surface covers under shadows had a reduced reflectance value [149], and this effect differed with the shadow level and hence influenced the LULC classification [46,70]. Shadow correction can increase classification accuracy remarkably in vegetation cover mapping over shaded areas, as demonstrated by Kumpumäki, et al. [40]; in their case the classification accuracy was increased from 35.1 to 46.1%.

A major LULC classification error was caused by spectral confusion among dark ISC, water bodies, and shadows from tree canopies among grassland or tall buildings in urban areas [151,152]. It is difficult to separate ISC from water, wetland, and shadows based solely on spectra, as shown in Figure 10 [153]. Spatial variation in the canopy caused by shadows significantly impacts pixel-based classification compared with object-based methods in fine resolution images [154].

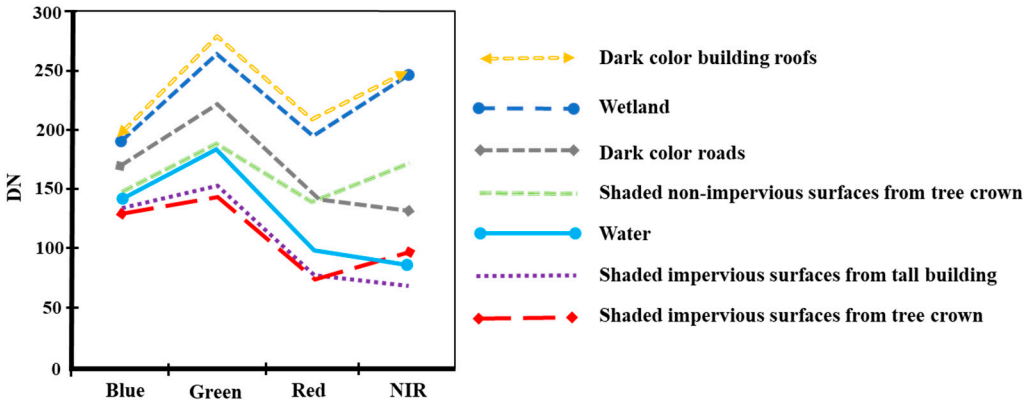

Figure 10. Comparison of different surface spectra in Quickbird imagery (adapted from [153]).

Shadows can have a negative impact on image classification results. It is important to assess this potential and to plan ideal satellite overpass times because shadows are extremely dependent on satellite overpass time and Sun angle [9,154].

3.2. Shadow Detection Methods

Shadow detection has always been relevant in image processing. This is because it provides useful information for various applications such as change detection, object extraction, classification, segmentation, and land monitoring [155]. Regarding this, many methods and algorithms were developed for shadow detection in remote sensing images. Based on these studies, shadow detection can be divided into four main categories: model-based, feature-based, index-based, and temporal differences.

3.2.1. Model-Based Methods

To simulate shadow areas, the model-based method utilizes a mathematical concept that relies on prior information. It applies information regarding the scene, moving objectives, the Sun and its elevation and azimuth, and the sensor's altitude to define shadow models. Aerial image analysis and video monitoring are two examples of applications where model-based methods are commonly used. The availability of prerequisite information can be a limitation in these methods [15,53,55,156].

3.2.2. Feature-Based Methods

Feature-based methods use the shadow specifications for shadow detection. There are some subtypes of this method: physical rule-based, object-based, invariant color spaces, and classification methods. The physical rule-based method uses image geometry (central

longitude and latitude), physical characteristics (altitude and temperature) and local time, shadow length and the position of the Sun. This method is also very efficient for moving shadow in video sequences [157]. F-mask is a rule-based method for detecting clouds and cloud shadows and is based on the physical characteristics of clouds [158].

The object-based method was developed based on the spectral characteristics of shadows (brightness and saturation) and texture. It is a widely used method for shadow detection [86] and applied mostly for urban areas as it can detect the edges of building shadow precisely [159]. The object-based method usually uses segmentation algorithms and has different subtypes: thresholding and region growing-based.

Thresholding is a quick and easy method which uses threshold values to divide pixels into different groups [15,28,87,160–164]. The threshold value is selected using different methods: Gaussian mixture model [165], arbitrarily by visual inspection [166], the number of peaks and valleys [87], and bimodal histogram splitting [159,164]. This method was improved by combining other spectral and spatial information [167]. Ghandour et al. [168] also introduced a method which is based on multi-thresholding. Their proposed model is called shadow detection multi-thresholding segmentation (SMS). This method is very accurate especially for building shadow detection

The region growing-based method uses the average and standard deviation of the pixels for classification. Each pixel is allocated to a potential segment based on spatial and spectral distance from that segment [169]. This method clusters the image iteratively and finds the shadow and non-shadow regions. The lowest pixel values are assigned to shadow and can be used as seeds for region growing. The method provides accurate segmentation results and has good performance in noisy areas [162].

Invariant color spaces methods are based on the luminance and chromaticity of invariant color space. Different color spaces with special properties (RGB, IHS, HSV, XYZ, YIQ, Luv, Lab, etc.) have been used for shadow detection. Shadows with specific characteristics such as larger saturation, larger hue values, and smaller brightness can be detected using the appropriate color space [15,67,160,163,170].

Classification methods are based on the properties of shadow pixels. Different classification methods were applied for shadow detection. Some of these methods are automatic while some are semi-automatic [171–175].

The most important advantage of unsupervised classification or clustering is its ability to be applied without human effort and automatic labeling [176]. Different unsupervised classification algorithms were used for shadow detection. K-means clustering was used widely in shadow detection. The initial number of classes must be determined based on spectral characteristics of the objects and the scene geometry [149,157]. However, this method is limited while using similar objects. A modified Gaussian mixture model was developed in this regard. To complete the spatial background modeling, a random number generation method was used to sample each pixel's neighborhood [59]. Movia, et al. [150] presented a method by using RGB color information for shadow detection. It might not be appropriate to use this method on cast shadows that are visible and correctly identified. Unsupervised machine learning is also very popular due to its quick and rough nature in shadow detection. Classes with the smallest values are considered as shadow [166].

Other classification methods include supervised- and object-based. To use these methods, training samples with identified spectra must be chosen. In light of this, supervised classification methods are usually costly and time-consuming [157]. Furthermore, supervised methods have some limitations, such as the lack of reference samples required for classifier training. It is also possible for trained classifiers to be insufficient for another scene [177]. Some methods were developed to overcome these problems [56,178].

Unlike unsupervised machine learning algorithm, training samples or ground reference data are used to build classifiers in supervised machine learning. This method, especially, the typical support vector machine (SVM), has been widely used in shadow detection [171–173]. Moreover, neural networks have been used for extracting spectral features in multiple levels from different bands and shadow detection was performed

based on these segmented features [179,180]. Deep learning methods, which are a subset of machine learning, were demonstrated to be efficient in some shadow detection studies [181]. Methods based on deep learning are very accurate in image classification, and this accuracy is continuously increasing with the development of new methods [182]. CNN [180,183], PCNN [179,180,183], U-Net CNN [6], MSCFF [6], and many other modified models have been introduced for shadow detection [184].

Recently, Yin, et al. [185] introduced a new self-supervised learning shadow detection algorithm for RS imagery. In this method, a shadow ratio threshold is generated automatically without human interaction. A self-supervised learning method was suggested by combining both supervised and unsupervised shadow detection methods. According to the results, this method is accurate and applicable for shadow detection.

3.2.3. Spectral Indices

Different methods have been developed based on various approaches to band selection. The methods are easy to practice and do not need any parameters [186,187]. Different indices were used for shadow detection. The Shadow Detection Index (SDI) is the most popular index for shadow detection based on optical bands. This method can discriminate shadow from dark objects and, therefore, is very accurate in shadow extraction. It is possible to visually identify the shadowed pixels, which allows a trial-and-error process to be used to determine the appropriate threshold value [157]. NDWI separates shadow pixels from water [158] and NDVI [188] separates shadow pixels from vegetation. The Combinational Shadow Index (CSI) can extract building shadows in urban areas. This method is efficient in both cloudy and clear conditions with high precision and works well on wide extent study areas. Shadows can be separated from water and low albedo features using CSI [54]. Sun et al. [54] developed the Normalized Saturation value Difference Index l (NSDVI) based on HSV color space for shadow detection. It chooses the area with greater saturation and lower density. These indices can be used in conjunction with other methods such as the support vector machine (SVM), maximum likelihood classifier (MLC), Otsus method, and histogram equalization method [15,160,170,189].

3.2.4. Temporal Differences

The temporal differences method compares multi-temporal images, such that images with different dates are used for shadow detection. Pixels with the largest differences are shadow [190–193]. Some methods have been developed for a specific sensor. In radar observations, shadows are mapped from modeled illumination with Mercury Dual Imaging System (MDIS) imagery and Mercury Laser Altimeter (MLA) data. Low reflectance surfaces can be detected using MLA reflectance at 1604 nm and radar bright deposits of MDIS. These two methods are independent, but can detect shadow simultaneously [194].

3.2.5. Advantages and Disadvantages

Qualitative and quantitative estimation of shadow regions can be greatly influenced by the method used. In previous studies, thresholding techniques were used widely for shadow detection due to their simplicity. However, a common problem with shadow detection methods based on thresholds is that shadow pixels are difficult to separate from non-shadow pixels, such as water, due to their similarity. The second more common method is modeling, which is simulates shadow regions based on prior information using a mathematical concept.

In comparison with thresholding methods, nonlinear shadow detection is very sensitive to shadow regions, but causes mixed pixels between shadow and non-shadow regions. It is possible to avoid this problem by using shadow detection methods based on shaded relief. However, these methods require highly accurate DEMs and they are unable to detect cast shadows as well. In Table 1, we summarize the different methods reviewed and their relative advantages and disadvantages.

Table 1. An overview of shadow detection methods.

Method	Brief Description	Advantage	Disadvantage
Thresholding	Spectral values have the key role in thresholding	Simple and quick	Cannot discriminate between non-shadow dark areas and shadow areas
Modeling	Location of the sensors, the light source direction and the observed objects geometry are the source of knowledge in shadow areas	Identifying the shadow regions with high accuracy	Source of light and scene Geometry are not vivid
Invariant color model	It is based on ratio of HSV or RGB bands	Identifying shadow regions from other dark objects	Misclassification which is due to uncertainty in certain color values.
Region growing segmentation	Cluster the image iteratively and find shadow and non-shadow regions.	Provides good segmentation results, performs well with respect to noise	Time-consuming
Shade relief	Solar elevation, solar zenith, and DEM are the key elements of this technique	Simple nature	Not calculate shadow that is cast by topographic features onto surrounding surface
Radar observations	(MDIS) images and modelled illumination with (MLA) topographic data are used	Detecting low reluctance surfaces at 1604 nm	Poor spatial resolution
Shadow Detection Index (SDI)	Three bands are utilized to establish a new spectral index	Simple, distinguishing dark object from shadows	Cannotextract the small portion of shadow
MSS clear-view mask (MSScvm)	A rule-based algorithm for identifying shadow in MSS data	Automatic, simple. Commission and omission errors are minimized	Customized only for MSS data
Sub-Pixel Shadow Mapping	Sub-pixel method is used for shadow detection	Mapping shadow with finer resolution. Preserving memory and fill rate consumption	Aliasing problems can be happened due to close-up on the shadow
Blackbody Radiator Model	Shadow is detected based on the chromaticity values	High accuracy	Medium complexity
The automatic cloud/shadow detection method	Use MRF method for detection	It is a simple image processing algorithm	Preprocessing is needed for clouds
Neural network and Pulse coupled neural networks (PCNN)	Based on neural network	Good shadow simulation	While hue and intensity of shadow and non-shadow region is similar, they can be miss classified
Object-Based shadow extraction	Shadow is detected as an object	More accurate than pixel-based methods spatially for bright objects	Dependent on the radiometric resolution of the sensor
Airborne Laser Scanner (ALS)	DSM is used for shadow simulation	Accurate	Data are rare, expensive, requires aircraft use,
Visual interpretation	Shadow is detected by interpreter	Easy to use	Dependent on the interpreter experience
Machine learning methods	Uses machine learning algorithms	Efficient	High computational cost and time

3.3. De-Shadowing Methods

It is possible to restore the brightness difference between shadowed and non-shadowed areas by de-shadowing. Although shadow degradation is easily detected by the human visual system [184] shadows are a major problem in computer image processing for images

with medium and fine spatial resolutions [27,55,195]. Research in recent years has focused mainly on restoring shadow data, rather than eliminating or reducing its effects [28,196,197]. Shadow can be restored using the useful information from the weak recorded reflectance in shadow regions [28,189,198] or using spatial information from non-shadow areas [196,199].

3.3.1. Urban Shadow Compensation

Five techniques were introduced in recent years for restoring shadow in urban environments. These include gamma correction, linear correlation correction (LCC), ratioing method, histogram matching, and multisource data fusion.

LCC defines shadow as the result of a combination of multiplicative and additive noises. To enhance the brightness of shadows, a linear relationship was used. Different pairs of pixels from similar surfaces have been used to obtain the function parameter in non-shadow and shadow areas. This method is efficient and can provide good results despite weak signals in shadow areas [67,118,166]. However, in the gamma correction method, shadow is considered as a multiplicative noise source which can corrupt the underlying pixel brightness. The gamma parameter was calculated from values of non-shadowed and shadowed pixels. According to research, this method is helpful for precise land use mapping especially when the image is split into smaller sections and more than one gamma value is used [200]. However, if the shadow is large and different types of surfaces have been applied, shadow classification and gamma value extraction is very difficult [197].

One common method used in many urban studies for shadow compensation is histogram matching. This method matches the histograms of shadowed and non-shadow areas of the same class in a way that makes them as similar as possible [160,201]. In a histogram matching area, window size is critical and must be taken into precise consideration [67,189]. Moreover, urban shadow can be compensated by increasing the pixel values of each spectral band via the band ratio method. Shadowed pixels are restored to their original brightness based on the average intensity ratio of shadowed and non-shadowed pixels for each class. Although very effective, spectral resolution is lost in this method [199].

In some studies, shadow pixels were simply replaced by non-shadow pixels of the same area, but different dates through multi-source or multi-temporal data fusion [202]. Fine spatial resolution images can be used for this purpose with some limitations, due to their coarse temporal resolution. Precise co-registration is of significant importance when using this method as it can lead to major errors. Although no information in shadow regions is missed, this method is not efficient for small cloudy regions [203].

3.3.2. Topographic Shadow Compensation

In high relief regions such as mountainous environments, topography blocks direct solar radiation, causing cast shadows. Solar elevation and landscape topography can change the amount of cast shadow at the acquisition time [67,160]. When using automated classifiers, cast shadows may not be taken into account, leading to classification errors [204]. Three main methods have been applied for topographic or terrain shadow correction. The simplest method is the band ratio. In this method, a single band is divided by another band [67]. It is important to note that this method is very common for all spatial resolutions (low, medium, and high) since it does not take into consideration varying illumination conditions and shadowing effects that are caused by variations in solar and viewing angles. Non-linear additive noise can affect the result as this method is not linear. Some vegetation indices such as EVI may encounter error due to the effects of topography [15]. Jiang et al. (2019) determined that the shadow-eliminated vegetation index (SEVI) can be calculated with only the reflectance of red and near-infrared bands without further information. Using SEVI, terrain shadow effects in both self and cast shadows can be eliminated with higher accuracy than with DEM-based correction methods, particularly in cast shadows [205].

In another method for topographic shadow compensation, the Hyper-Spherical Direction Cosine Transformation (HSDC) transforms measurement vectors onto a hypersphere by splitting pixel vectors into illumination/albedo and spectral components. HSDC transfor-

mation is appropriate for removing topographic effects and has some limitations due to losing information during transformation [67]. The third category of methods for topographic shadow compensation are the Digital Elevation Model (DEM)-based methods. These methods can be categorized into three general categories: Lambertian, non-Lambertian, and empirical methods [206]. The most frequently DEM-based Lambertian methods introduced by researchers are: the Sun-canopy-sensor method, C correction, variable empirical coefficient algorithm (VECA), Minnaert correction, and Lambert cosine correction.

Cosine correction is a straightforward process that requires only terrain illumination data and solar zenith angle. This method, however, does not take into account diffuse illumination, which can account for a considerable amount of irradiance on slopes facing away from the Sun and within the forest canopy [207,208]. The C correction is an improved version of a cosine correction formulation [207,208]. Multitemporal images taken in different illumination conditions can benefit from using this method for radiometric correction [209,210].

Another DEM-based method is Minnaert correction. The Minnaert constant was adopted by Smith et al. [211] for correcting topographic effects based on a formula proposed by Minnaert [212]. It is possible to use this method to describe whether or not a surface is near an ideal diffuse reflector. Minnaert constants change with the cosine of the incidence angle [213]. This method not only yielded better results than the simple cosine correction (e.g., Meyer et al. [214], Ekstand [213]), but also did not allow for parameterizing the skylight irradiance.

A Sun-canopy-sensor (SCS) model was applied for de-shadowing in some studies. It is extremely efficient in correcting terrain in forests because it preserves the position of the Sun, sensor orientation, geometry, and canopy structure as well as normalizing the amount of sunlight within each pixel [215]. As a means of accounting for diffuse radiation, a semi-empirical moderator (C) was introduced to this method [13]. In addition, these models cannot be used to classify vegetation surfaces in rugged terrain, nor can they fully explain the relationship between crown structure, shadow, terrain, and mutual shadowing within forest and tree canopies [216]. For each pixel, a method for determining the shadow boundary and sky view factor (SVF) was developed. DEM and Sun position are used in this model to reconstruct the geometric relationship between land surfaces. Based on the SVF of each pixel, a ground radiative transfer model is then constructed to determine the lost radiation of each shadow pixel. For this model, scattering and direct radiation are used along with a ground multiple reflectance constant [217]. Furthermore, a variational framework based on cast shadows (CSVF) was proposed by Li et al. (2016) for improving the topographic correction of the above-mentioned models. Through the correction of the radiometric distortion caused by cast shadows, which is neglected by the above-mentioned topographic correction models, the topographic correction results are improved [218].

3.3.3. Cloud Compensation

Clouds are common in remote sensing images. Optical sensors cannot retrieve information from underneath clouds because they do not receive any signal from the Earth. Clouds can, thus, reduce the amount of information that can be obtained from remote sensing images [219,220]. Sometimes, cloudy images are the only available data, so they must be used. Two main methods have been applied for cloud compensation. One of them is the multispectral-based method. Multispectral data are employed in this method to detect and restore clouds. As no tuning parameter is used in this method, it can be automated. Moreover, it is applied per pixel, so missed or contaminated pixels would not change the result [64]. Ordinary co-kriging and standardized ordinary co-kriging techniques have been proposed by Zhang, et al. [221] for intensity interpolation of cloud-contaminated pixels. Although this method is efficient for small clouds in non-homogeneous landscape, it is not appropriate for large size clouds. Another method is the multi-temporal-based method. This method uses both the spectral and spatial coherence of images and has better performance for large clouds [190]. This method can be used for replacing cloudy pixels

with cloudless pixels in a reference image. It is assumed that both cloudy and cloud-free image samples of each band have approximately the same average and standard deviation. As a result of the large difference between the real average and standard deviation and the estimated one, this method must be used with caution when using it for large clouds [222]. Wavelet image fusion was also applied in this regard and is rarely efficient for small clouds as it cannot detect small cloud borders [66]. Solar geometry, sensor viewing computation, and co-registration are the main challenges associated with this method [64].

3.3.4. Compound Shadow Compensation

Compound shadow compensation methods have been used when more than one type of shadow is present in an image. Various cloud, topographic, and urban shadows appearing simultaneously lead to new conditions for de-shadowing [57,195]. Because of their unique characteristics, these methods are mostly used to correct certain types of shadows [223]. Some methods, however, can correct shadows of more than one type [67]. Linear correlation correction (LCC) is one of these methods, which is based on linear relationships and is mainly designed for urban shadows. It can also be applied to compensate for topographic and cloud shadows. Multisource data fusion is another method. This method was developed to remove cloud shadows from coarse spatial resolution images, but it can also be used on fine spatial resolution images of urban regions [191]. The Surface Reflectance Equality-Based Method is another widely used model for compound shadow compensation. In this method, a shadowed feature's surface reflectivity is assumed to be the same as a sunlit feature's surface. This method can restore cloud shadows, topographic shadows, and urban shadows.

While various types of shadows are present in the image, it is critical to know the first type of shadow that should be corrected. Regarding this, the significance of each type of shadow must be considered in compound shadow detection. Moreover, the affected area of the potential shadow objects is important [46]. Therefore, shadows of small objects are the last priority. On the contrary, cloud shadow is the first to be compensated [67].

3.3.5. Advantages and Disadvantages

The performance of various processes such as segmentation, classification, change detection, time series analysis, and object detection is improved when shadows are removed from images. As a preprocessing technique, shadow compensation can be applied to any RS processing chain. With regards to shadow compensation methods, these approaches vary depending on the kind of shadow and the type of sensor [28]. Several advantages and disadvantages are associated with each method.

With the band ratio method, it is possible to remove shadows regardless of the type of shadow [224]. Despite this, the method is not linear and can be affected by additive noise such as atmospheric path radiance. Moreover, topographic factors such as shadow may result in higher error rates for spectral indices with constant values [225]. Models based on topography (for topographic shadows), recovery approaches (for urban shadows), and wavelet transformations (for cloud shadows) appear to be the most promising options. However, there are some challenges with them: recovery methods in fine resolution images are time-consuming and manual, and models based on topography can be effective, but they can be complex to implement. In Table 2, we summarize the advantages and disadvantages of various de-shadowing methods.

Table 2. An overview of de-shadowing methods.

Method	Brief Description	Advantage	Disadvantage
Visual interpretation	Visual analysis-based,	Simple, quick, and easy process	Expensive, time-consuming
Band ratio indices	Uses band ratio	Very effective	Spectral resolution is lost
Multisource classification	Combination of DEM and vegetation indices	Topographic component is omitted	Accuracy and resolution of DEM can affect the result
Topographic correction models	Mathematical models-based	Normalizes area of sunlit canopy	Relationship between terrain and shadow is ambiguous
Recovery techniques	Mathematical models-based.	Simple Cost efficient	Problems with mixed pixels in complex landscapes
Data mining techniques	Recovering information from shadow regions using data mining	Information of shadow regions can be restored without removing them	Time-consuming and background issue
Histogram matching	Uses image processing techniques	The values of pixels covered by shadows can be recovered	Sensitive to window size
Multisource data fusion	Apply fusion techniques	Use information of two images	Limitation of image acquisition Time Image registration error
K-means clustering	Clustering-based	The edges of shadow can be precisely detected	Depended on the point distance measurement
inner outer outline profile line (Ioopl)	Statistic and thresholding-based	Use of Image statistical features	Dark objects may be misclassified as shadows
Microwave data	Use passive microwave data	Cloud-free imagery	Very low emitted energy, low resolution, large area should be imaged
Multisource fusion and Multi-date imager	Wavelet technique Fusion	No information in shadow regions is missed	Inefficient for small cloudy regions
Unmixing	Used concept of unmixing	Using information of shadow regions as endmember	Skylight diffusion is neglected while collecting endmember
Gamma correction techniques	Use gamma parameter for shadow detection	Useful for accurate land use mapping	A single gamma parameter is used Time-consuming

4. Discussion

Two processing operations are required to correct shadows: shadow detection and de-shadowing. There are several factors that determine whether shadow correction is successful. Some of these factors include the type of shadow, and the type and spatial resolution of the sensor that was used for image acquisition. To create images that do not contain shadows or at least minimize the impact of shadows, an appropriate method for detecting and de-shadowing shadows is necessary.

Future Research Directions

The detection of shadow effects is rarely studied, despite the fact that many studies have been undertaken to improve shadow detection methods. In future research, it should be possible to distinguish between self-shadow and shadow effects on surface biophysical variables measured by remote sensing. As part of this study, we attempted to provide a better understanding of how shadows affect surface biophysical variables derived from remote sensing. More research is needed in the future to quantify the shadow effects on each of these variables. Moreover, in previous studies, the effect of different shadow types including urban, cloud, and topography on the surface biophysical variables was

not evaluated. It is suggested that the effect of the shadow type on the surface biophysical variables and differences in their effects should be highlighted.

It is possible to enhance existing methods (or implement novel ones) based on the advantages and drawbacks of shadow detection and compensation methods as discussed earlier. In general, shadow correction methods (detecting and de-shadowing) must be quick, reliable, and automatic. Moreover, it is worthwhile to note that most of these methods should reduce the effect of mixed pixels between shadow regions and similar classes such as buildings, water bodies, and forests to minimize the uncertainty of LULC classification or other remote sensing applications due to shadows. In future developments, it is recommended to purify the information in the shadows as much as possible rather than remove or lose it completely.

Several aforementioned studies have indicated that shadow can be defined as abnormal/noisy areas within fine and medium resolution remote sensing data, specifically topographic shadow and urban shadow. Therefore, integrating target/outlier detection methods may be a more effective approach to detecting the location of shadow areas than simply thresholding. However, several studies have referred to shadow regions as missing areas within a remote sensing dataset. It is possible to fill shadow pixels in images using traditional interpolation methods, for example bilinear interpolation, but these methods may not be appropriate for this purpose. This is because these methods consider uniform variation across the entire image. Despite this, remote sensing images contain spatial structure and spectral information is commonly not uniform across a study area. Several other approaches should be considered in future research, including spatial autocorrelation-based geostatistical methods or feature correlation-based machine learning methods to retrieve missing values in shadow areas and predict information in the corresponding regions. Future research should also focus on developing effective methods for compound shadow compensation.

5. Conclusions

Shadows can have a substantial undesirable effect on RS data. Therefore, recognizing and modeling the effect of shadows on RS data and the information that may be extracted from them is important for environmental analysis. Shadows were classified into four categories: cloud shadows, topographic shadows, urban shadows, and a combination of these effects. These shadows can complicate the analysis of coarse, medium, and fine spatial resolution imagery. The effect of shadows on various variables is a function of the sensor and Sun geometry, the satellite's overpass time, and the spatial resolution of the images.

This review shows that shadows can affect a wide variety of properties including those related to vegetation, ISC, water, snow, albedo, SM, transpiration, evaporation, LST, urban heat island, LULC maps, and surface coatings. Shadows can reduce the quantity and quality of information obtained from these various properties while increasing errors and uncertainty in subsequent analyses. Considering these indirect and direct effects of shadows on the extraction of properties from remote sensing images, developing effective algorithms for identifying and correcting shadow effects is of paramount importance. Moreover, the choice of the most suitable type of method to identify and correct shadow effects is important in terms of the resulting effect on both qualitative and quantitative accuracy.

Most recent studies have attempted to retrieve information or to reduce the effects of shadowed areas instead of omitting these areas in further analysis. This is especially true for ultra-fine spatial resolution UAV images. Shadows in ultra-fine resolution data may have a different character and heterogeneity to those in the more common fine, moderate, and coarse spatial resolution satellite sensor imagery. There exist several ways to identify and correct shadow effects in RS images, but there is no universal way to correct all shadows (i.e., cloud shadows, shadows of urban phenomena, and topographical shadows). This is because every shadow type has its own characteristics such that specific correction techniques are required in each case. There is a growing demand for machine learning-

based methods to reduce the effects of shadows with promising results, and this avenue should be explored further for a range of shadow types and different contexts.

Author Contributions: Conceptualization, S.K.A., M.K.F. and A.S.; methodology, M.K.F., A.S., S.F., Z.G. and M.N.; writing—original draft preparation, M.K.F., A.S., S.F., S.Z.N., S.S., Z.G. and M.N.; writing—review and editing, S.K.A., J.J.A., M.M., S.Q., Q.W., D.H., B.P., A.B. and P.M.A.; project administration, S.K.A.; funding acquisition, J.J.A. and S.K.A. All authors have read and agreed to the published version of the manuscript.

Funding: This research received no external funding.

Data Availability Statement: The data used to support the findings of this study are available from the corresponding author upon reasonable request.

Acknowledgments: The authors thank anonymous reviewers for their constructive comments and suggestions which helped to improve the manuscript. This study was supported by the Iran National Science Foundation (Grant No. 96003646), and Agrohydrology Research Group of Tarbiat Modares University (Grant No. IG-39713).

Conflicts of Interest: The authors declare no conflict of interest.

References

1. Xue, J.; Su, B. Significant remote sensing vegetation indices: A review of developments and applications. *J. Sens.* **2017**, *2017*, 1353691. [CrossRef]
2. Mahabir, R.; Croitoru, A.; Crooks, A.; Agouris, P.; Stefanidis, A. A critical review of high and very high-resolution remote sensing approaches for detecting and mapping slums: Trends, challenges and emerging opportunities. *Urban Sci.* **2018**, *2*, 8. [CrossRef]
3. Chen, G.; Weng, Q.; Hay, G.J.; He, Y. Geographic Object-based Image Analysis (GEOBIA): Emerging trends and future opportunities. *GIScience Remote Sens.* **2018**, *55*, 159–182. [CrossRef]
4. Mather, P.; Tso, B. *Classification Methods for Remotely Sensed Data*; CRC Press: Boca Raton, FL, USA, 2016.
5. Huang, C.; Chen, Y.; Zhang, S.; Wu, J. Detecting, extracting, and monitoring surface water from space using optical sensors: A review. *Rev. Geophys.* **2018**, *56*, 333–360. [CrossRef]
6. Wieland, M.; Li, Y.; Martinis, S. Multi-sensor cloud and cloud shadow segmentation with a convolutional neural network. *Remote Sens. Environ.* **2019**, *230*, 111203. [CrossRef]
7. Zekoll, V.; Main-Knorn, M.; Alonso, K.; Louis, J.; Frantz, D.; Richter, R.; Pflug, B. Comparison of masking algorithms for sentinel-2 imagery. *Remote Sens.* **2021**, *13*, 137. [CrossRef]
8. Wu, S.; Wen, J.; Gastellu-Etchegorry, J.-P.; Liu, Q.; You, D.; Xiao, Q.; Hao, D.; Lin, X.; Yin, T. The definition of remotely sensed reflectance quantities suitable for rugged terrain. *Remote Sens. Environ.* **2019**, *225*, 403–415. [CrossRef]
9. Milas, A.S.; Arend, K.; Mayer, C.; Simonson, M.A.; Mackey, S. Different colours of shadows: Classification of UAV images. *Int. J. Remote Sens.* **2017**, *38*, 3084–3100. [CrossRef]
10. Paul, A.; Chowdary, V.; Srivastava, Y.; Dutta, D.; Sharma, J. Change detection of linear features in temporally spaced remotely sensed images using edge-based grid analysis. *Geocarto Int.* **2017**, *32*, 640–654. [CrossRef]
11. Jin, H.; Li, A.; Xu, W.; Xiao, Z.; Jiang, J.; Xue, H. Evaluation of topographic effects on multiscale leaf area index estimation using remotely sensed observations from multiple sensors. *ISPRS J. Photogramm. Remote Sens.* **2019**, *154*, 176–188. [CrossRef]
12. Wen, J.; Liu, Q.; Xiao, Q.; Liu, Q.; You, D.; Hao, D.; Wu, S.; Lin, X. Characterizing land surface anisotropic reflectance over rugged terrain: A review of concepts and recent developments. *Remote Sens.* **2018**, *10*, 370. [CrossRef]
13. Soenen, S.A.; Peddle, D.R.; Coburn, C.A. SCS + C: A modified sun-canopy-sensor topographic correction in forested terrain. *IEEE Trans. Geosci. Remote Sens.* **2005**, *43*, 2148–2159. [CrossRef]
14. Sandmeier, S.; Itten, K.I. A physically-based model to correct atmospheric and illumination effects in optical satellite data of rugged terrain. *IEEE Trans. Geosci. Remote Sens.* **1997**, *35*, 708–717. [CrossRef]
15. Shahtahmassebi, A.; Yang, N.; Wang, K.; Moore, N.; Shen, Z. Review of shadow detection and de-shadowing methods in remote sensing. *Chin. Geogr. Sci.* **2013**, *23*, 403–420. [CrossRef]
16. Huang, X.; Wang, Y. Investigating the effects of 3D urban morphology on the surface urban heat island effect in urban functional zones by using high-resolution remote sensing data: A case study of Wuhan, Central China. *ISPRS J. Photogramm. Remote Sens.* **2019**, *152*, 119–131. [CrossRef]
17. Shettigara, V.; Sumerling, G. Height determination of extended objects using shadows in SPOT images. *Photogramm. Eng. Remote Sens.* **1998**, *64*, 35–43.
18. Huang, Z.; Wang, F.; You, H.; Hu, Y. STC-Det: A Slender Target Detector Combining Shadow and Target Information in Optical Satellite Images. *Remote Sens.* **2021**, *13*, 4183. [CrossRef]
19. Nair, V.; Ram, P.G.K.; Sundararaman, S. Shadow detection and removal from images using machine learning and morphological operations. *J. Eng.* **2019**, *2019*, 11–18. [CrossRef]

20. Yang, X.; Chen, L. Evaluation of automated urban surface water extraction from Sentinel-2A imagery using different water indices. *J. Appl. Remote Sens.* **2017**, *11*, 026016. [CrossRef]
21. Liu, D.; Zhang, J.; Wu, Y.; Zhang, Y. A shadow detection algorithm based on multiscale spatial attention mechanism for aerial remote sensing images. *IEEE Geosci. Remote Sens. Lett.* **2021**, *19*, 6003905. [CrossRef]
22. Wójcik-Długoborska, K.A.; Bialik, R.J. The influence of shadow effects on the spectral characteristics of glacial meltwater. *Remote Sens.* **2020**, *13*, 36. [CrossRef]
23. Simpson, J.J.; Stitt, J.R. A procedure for the detection and removal of cloud shadow from AVHRR data over land. *IEEE Trans. Geosci. Remote Sens.* **1998**, *36*, 880–897. [CrossRef]
24. Kour, R.; Patel, N.; Krishna, A.P. Influence of shadow on the thermal and optical snow indices and their interrelationship. *Remote Sens. Environ.* **2016**, *187*, 119–129. [CrossRef]
25. Fisher, A.; Flood, N.; Danaher, T. Comparing Landsat water index methods for automated water classification in eastern Australia. *Remote Sens. Environ.* **2016**, *175*, 167–182. [CrossRef]
26. Caggiano, M.D.; Tinkham, W.T.; Hoffman, C.; Cheng, A.S.; Hawbaker, T.J. High resolution mapping of development in the wildland-urban interface using object based image extraction. *Heliyon* **2016**, *2*, e00174. [CrossRef]
27. Saha, A.; Arora, M.; Csaplovics, E.; Gupta, R. Land cover classification using IRS LISS III image and DEM in a rugged terrain: A case study in Himalayas. *Geocarto Int.* **2005**, *20*, 33–40. [CrossRef]
28. Liu, W.; Yamazaki, F. Object-based shadow extraction and correction of high-resolution optical satellite images. *IEEE J. Sel. Top. Appl. Earth Obs. Remote Sens.* **2012**, *5*, 1296–1302. [CrossRef]
29. Luo, H.; Wang, L.; Wu, C.; Zhang, L. An improved method for impervious surface mapping incorporating LiDAR data and high-resolution imagery at different acquisition times. *Remote Sens.* **2018**, *10*, 1349. [CrossRef]
30. Huang, F.; Yu, Y.; Feng, T. Automatic extraction of impervious surfaces from high resolution remote sensing images based on deep learning. *J. Vis. Commun. Image Represent.* **2019**, *58*, 453–461. [CrossRef]
31. Zhang, L.; Sun, X.; Wu, T.; Zhang, H. An analysis of shadow effects on spectral vegetation indexes using a ground-based imaging spectrometer. *IEEE Geosci. Remote Sens. Lett.* **2015**, *12*, 2188–2192. [CrossRef]
32. Peng, W.; Zhou, J.; Wen, L.; Xue, S.; Dong, L. Land surface temperature and its impact factors in Western Sichuan Plateau, China. *Geocarto Int.* **2017**, *32*, 919–934. [CrossRef]
33. Wang, T.; Shi, J.; Ma, Y.; Husi, L.; Comyn-Platt, E.; Ji, D.; Zhao, T.; Xiong, C. Recovering land surface temperature under cloudy skies considering the solar-cloud-satellite geometry: Application to MODIS and Landsat-8 data. *J. Geophys. Res. Atmos.* **2019**, *124*, 3401–3416. [CrossRef]
34. Wang, T.; Shi, J.; Husi, L.; Zhao, T.; Ji, D.; Xiong, C.; Gao, B. Effect of solar-cloud-satellite geometry on land surface shortwave radiation derived from remotely sensed data. *Remote Sens.* **2017**, *9*, 690. [CrossRef]
35. Renhua, Z.; Hongbo, S.; Zhaoliang, L.; Xiaomin, S.; Xinzhai, T.; Becker, F. The potential information in the temperature difference between shadow and sunlit of surfaces and a new way of retrieving the soil moisture. *Sci. China Ser. D Earth Sci.* **2001**, *44*, 112–123. [CrossRef]
36. Xie, C.; Huang, X.; Zeng, W.; Fang, X. A novel water index for urban high-resolution eight-band WorldView-2 imagery. *Int. J. Digit. Earth* **2016**, *9*, 925–941. [CrossRef]
37. Villegas, J.C.; Breshears, D.D.; Zou, C.B.; Royer, P.D. Seasonally pulsed heterogeneity in microclimate: Phenology and cover effects along deciduous grassland–forest continuum. *Vadose Zone J.* **2010**, *9*, 537–547. [CrossRef]
38. Feng, Y.; Qiu, G.Y.; Zhang, Q. Determination of canopy-shadow-affected area in sparse steppes and its effects on evaporation and evapotranspiration. *Ecohydrology* **2014**, *7*, 1589–1603. [CrossRef]
39. Wu, S.-T.; Hsieh, Y.-T.; Chen, C.-T.; Chen, J.-C. A Comparison of 4 shadow compensation techniques for land cover classification of shaded areas from high radiometric resolution aerial images. *Can. J. Remote Sens.* **2014**, *40*, 315–326. [CrossRef]
40. Kumpumäki, T.; Lipping, T. Effects of shadow correction on vegetation and land cover classification from high resolution aerial images. In Proceedings of the 2016 IEEE International Geoscience and Remote Sensing Symposium (IGARSS), Beijing, China, 10–15 July 2016; pp. 751–754.
41. Kulkarni, A.; Singh, S.; Mathur, P.; Mishra, V. Algorithm to monitor snow cover using AWiFS data of RESOURCESAT-1 for the Himalayan region. *Int. J. Remote Sens.* **2006**, *27*, 2449–2457. [CrossRef]
42. Cherubini, F.; Vezhapparambu, S.; Bogren, W.; Astrup, R.; Strømman, A.H. Spatial, seasonal, and topographical patterns of surface albedo in Norwegian forests and cropland. *Int. J. Remote Sens.* **2017**, *38*, 4565–4586. [CrossRef]
43. Cao, C.; Lee, X.; Muhlhausen, J.; Bonneau, L.; Xu, J. Measuring landscape albedo using unmanned aerial vehicles. *Remote Sens.* **2018**, *10*, 1812. [CrossRef]
44. Ozdemir, I. Estimating stem volume by tree crown area and tree shadow area extracted from pan-sharpened Quickbird imagery in open Crimean juniper forests. *Int. J. Remote Sens.* **2008**, *29*, 5643–5655. [CrossRef]
45. Kolzenburg, S.; Favalli, M.; Fornaciai, A.; Isola, I.; Harris, A.; Nannipieri, L.; Giordano, D. Rapid updating and improvement of airborne LIDAR DEMs through ground-based SfM 3-D modeling of volcanic features. *IEEE Trans. Geosci. Remote Sens.* **2016**, *54*, 6687–6699. [CrossRef]
46. Zhou, W.; Huang, G.; Troy, A.; Cadenasso, M. Object-based land cover classification of shaded areas in high spatial resolution imagery of urban areas: A comparison study. *Remote Sens. Environ.* **2009**, *113*, 1769–1777. [CrossRef]

47. Xie, Y.; Feng, D.; Xiong, S.; Zhu, J.; Liu, Y. Multi-scene building height estimation method based on shadow in high resolution imagery. *Remote Sens.* **2021**, *13*, 2862. [CrossRef]
48. Hou, W.-m.; Chen, X.-m.; Zhao, J.; Han, J. A shadow information recovery technology in 3D visualization of urban remote sensing images. In Proceedings of the AOPC 2021: Optical Sensing and Imaging Technology, Beijing, China, 23–25 June 2021; pp. 233–238.
49. Vélez, S.; Poblete-Echeverría, C.; Rubio, J.A.; Barajas, E. Estimation of Leaf Area Index in vineyards by analysing projected shadows using UAV imagery. *OENO One* **2021**, *55*, 159–180. [CrossRef]
50. Azevedo, S.; Silva, E.; Pedrosa, M. Shadow Detection Improvement Using Spectral Indices and Morphological Operators in Urban Areas in High Resolution Images. *Int. Arch. Photogramm. Remote Sens. Spat. Inf. Sci.* **2015**, *40*, 587–592. [CrossRef]
51. Bouziani, M.; Goïta, K.; He, D.-C. Automatic change detection of buildings in urban environment from very high spatial resolution images using existing geodatabase and prior knowledge. *ISPRS J. Photogramm. Remote Sens.* **2010**, *65*, 143–153. [CrossRef]
52. Blesius, L.; Weirich, F. The use of the Minnaert correction for land-cover classification in mountainous terrain. *Int. J. Remote Sens.* **2005**, *26*, 3831–3851. [CrossRef]
53. Zhou, K.; Lindenbergh, R.; Gorte, B. Automatic Shadow Detection in Urban Very-High-Resolution Images Using Existing 3D Models for Free Training. *Remote Sens.* **2019**, *11*, 72. [CrossRef]
54. Sun, G.; Huang, H.; Weng, Q.; Zhang, A.; Jia, X.; Ren, J.; Sun, L.; Chen, X. Combinational shadow index for building shadow extraction in urban areas from sentinel-2a msi imagery. *Int. J. Appl. Earth Obs. Geoinf.* **2019**, *78*, 53–65. [CrossRef]
55. Zhan, Q.; Shi, W.; Xiao, Y. Quantitative analysis of shadow effects in high-resolution images of urban areas. *Int. Arch. Photogramm. Remote Sens.* **2005**, *36*, 1–6.
56. Zhou, T.; Fu, H.; Sun, C.; Wang, S. Shadow detection and compensation from remote sensing images under complex urban conditions. *Remote Sens.* **2021**, *13*, 699. [CrossRef]
57. Liu, Y.; Wei, Y.; Tao, S.; Dai, Q.; Wang, W.; Wu, M. Object-oriented detection of building shadow in TripleSat-2 remote sensing imagery. *J. Appl. Remote Sens.* **2020**, *14*, 036508. [CrossRef]
58. Han, H.; Han, C.; Xue, X.; Hu, C.; Huang, L.; Li, X.; Lan, T.; Wen, M. A Mixed Property-Based Automatic Shadow Detection Approach for VHR Multispectral Remote Sensing Images. *Appl. Sci.* **2018**, *8*, 1883. [CrossRef]
59. Xia, H.; Song, S.; He, L. A modified Gaussian mixture background model via spatiotemporal distribution with shadow detection. *Signal Image Video Process.* **2016**, *10*, 343–350. [CrossRef]
60. Zhang, Q.; Yang, L.T.; Chen, Z.; Li, P. PPHOPCM: Privacy-preserving high-order possibilistic c-means algorithm for big data clustering with cloud computing. *IEEE Trans. Big Data* **2017**, *8*, 25–34. [CrossRef]
61. Zhang, Q.; Yang, L.T.; Chen, Z.; Li, P. A survey on deep learning for big data. *Inf. Fusion* **2018**, *42*, 146–157. [CrossRef]
62. Zhu, Z.; Wang, S.; Woodcock, C.E. Improvement and expansion of the Fmask algorithm: Cloud, cloud shadow, and snow detection for Landsats 4–7, 8, and Sentinel 2 images. *Remote Sens. Environ.* **2015**, *159*, 269–277. [CrossRef]
63. Mohajerani, S.; Saeedi, P. Cloud and cloud shadow segmentation for remote sensing imagery via filtered jaccard loss function and parametric augmentation. *IEEE J. Sel. Top. Appl. Earth Obs. Remote Sens.* **2021**, *14*, 4254–4266. [CrossRef]
64. Roy, D.P.; Ju, J.; Lewis, P.; Schaaf, C.; Gao, F.; Hansen, M.; Lindquist, E. Multi-temporal MODIS–Landsat data fusion for relative radiometric normalization, gap filling, and prediction of Landsat data. *Remote Sens. Environ.* **2008**, *112*, 3112–3130. [CrossRef]
65. de Carvalho, L.M.T. *Mapping and Monitoring Forest Remnants: A Multiscale Analysis of Spatio-Temporal Data*; Wageningen University and Research ProQuest Dissertations Publishing: Ann Arbor, MI, USA, 2001.
66. Arellano, P. Missing Information in Remote Sensing: Wavelet Approach to Detect and Remove Clouds and Their Shadows. Master's Thesis, International Institute for Geo-Information Scince and Earth Observation, Enschede, The Netherlands, 2003.
67. Mostafa, Y. A review on various shadow detection and compensation techniques in remote sensing images. *Can. J. Remote Sens.* **2017**, *43*, 545–562. [CrossRef]
68. Pickering, C.; Byrne, J. The benefits of publishing systematic quantitative literature reviews for PhD candidates and other early-career researchers. *High. Educ. Res. Dev.* **2014**, *33*, 534–548. [CrossRef]
69. Hoque, M.A.-A.; Phinn, S.; Roelfsema, C. A systematic review of tropical cyclone disaster management research using remote sensing and spatial analysis. *Ocean Coast. Manag.* **2017**, *146*, 109–120. [CrossRef]
70. Lu, D.; Hetrick, S.; Moran, E. Impervious surface mapping with Quickbird imagery. *Int. J. Remote Sens.* **2011**, *32*, 2519–2533. [CrossRef] [PubMed]
71. Hao, D.; Wen, J.; Xiao, Q.; Wu, S.; Lin, X.; Dou, B.; You, D.; Tang, Y. Simulation and analysis of the topographic effects on snow-free albedo over rugged terrain. *Remote Sens.* **2018**, *10*, 278. [CrossRef]
72. Wen, J.; Zhao, X.; Liu, Q.; Tang, Y.; Dou, B. An improved land-surface albedo algorithm with DEM in rugged terrain. *IEEE Geosci. Remote Sens. Lett.* **2013**, *11*, 883–887.
73. Wen, J.; Liu, Q.; Liu, Q.; Xiao, Q.; Li, X. Scale effect and scale correction of land-surface albedo in rugged terrain. *Int. J. Remote Sens.* **2009**, *30*, 5397–5420. [CrossRef]
74. Li, H.; Shen, Y.; Yang, P.; Zhao, W.; Allen, R.G.; Shao, H.; Lei, Y. Calculation of albedo on complex terrain using MODIS data: A case study in Taihang Mountain of China. *Environ. Earth Sci.* **2015**, *74*, 6315–6324. [CrossRef]
75. Lee, S.-H.; Ahn, J.-S.; Kim, S.-W.; Kim, H.-D. Multiple Albedo Variation Caused by the Shadow Effect of Urban Building and Its Impacts on the Urban Surface Heat Budget. *J. Korean Earth Sci. Soc.* **2010**, *31*, 738–748. [CrossRef]
76. Schaaf, C.B.; Li, X.; Strahler, A.H. Topographic effects on bidirectional and hemispherical reflectances calculated with a geometric-optical canopy model. *IEEE Trans. Geosci. Remote Sens.* **1994**, *32*, 1186–1193. [CrossRef]

77. Gao, B.; Jia, L.; Menenti, M. An improved method for retrieving land surface albedo over rugged terrain. *IEEE Geosci. Remote Sens. Lett.* **2013**, *11*, 554–558. [CrossRef]
78. Petropoulos, G.P.; Maltese, A.; Carlson, T.N.; Provenzano, G.; Pavlides, A.; Ciraolo, G.; Hristopulos, D.; Capodici, F.; Chalkias, C.; Dardanelli, G. Exploring the use of Unmanned Aerial Vehicles (UAVs) with the simplified 'triangle'technique for soil water content and evaporative fraction retrievals in a Mediterranean setting. *Int. J. Remote Sens.* **2021**, *42*, 1623–1642. [CrossRef]
79. Lu, D.; Weng, Q. Extraction of urban impervious surfaces from an IKONOS image. *Int. J. Remote Sens.* **2009**, *30*, 1297–1311. [CrossRef]
80. Weng, Q. Remote sensing of impervious surfaces in the urban areas: Requirements, methods, and trends. *Remote Sens. Environ.* **2012**, *117*, 34–49. [CrossRef]
81. Wang, Y.; Su, H.; Li, M. An Improved Model Based Detection of Urban Impervious Surfaces Using Multiple Features Extracted from ROSIS-3 Hyperspectral Images. *Remote Sens.* **2019**, *11*, 136. [CrossRef]
82. Firozjaei, M.K.; Fathololoumi, S.; Kiavarz, M.; Biswas, A.; Homaee, M.; Alavipanah, S.K. Land Surface Ecological Status Composition Index (LSESCI): A novel remote sensing-based technique for modeling land surface ecological status. *Ecol. Indic.* **2021**, *123*, 107375. [CrossRef]
83. Firozjaei, M.K.; Kiavarz, M.; Homaee, M.; Arsanjani, J.J.; Alavipanah, S.K. A novel method to quantify urban surface ecological poorness zone: A case study of several European cities. *Sci. Total Environ.* **2021**, *757*, 143755. [CrossRef]
84. Firozjaei, M.K.; Sedighi, A.; Argany, M.; Jelokhani-Niaraki, M.; Arsanjani, J.J. A geographical direction-based approach for capturing the local variation of urban expansion in the application of CA-Markov model. *Cities* **2019**, *93*, 120–135. [CrossRef]
85. Lin, Y.; Zhang, H.; Li, G.; Wang, T.; Wan, L.; Lin, H. Improving Impervious Surface Extraction with Shadow-Based Sparse Representation from Optical, SAR, and LiDAR Data. *IEEE J. Sel. Top. Appl. Earth Obs. Remote Sens.* **2019**, *12*, 2417–2428. [CrossRef]
86. Yang, J.; He, Y. Automated mapping of impervious surfaces in urban and suburban areas: Linear spectral unmixing of high spatial resolution imagery. *Int. J. Appl. Earth Obs.* **2017**, *54*, 53–64. [CrossRef]
87. Chen, Y.; Wen, D.; Jing, L.; Shi, P. Shadow information recovery in urban areas from very high resolution satellite imagery. *Int. J. Remote Sens.* **2007**, *28*, 3249–3254. [CrossRef]
88. Xian, G.; Shi, H.; Dewitz, J.; Wu, Z. Performances of WorldView 3, Sentinel 2, and Landsat 8 data in mapping impervious surface. *Remote Sens. Appl. Soc. Environ.* **2019**, *15*, 100246. [CrossRef]
89. Tang, F.; Xu, H. Impervious Surface Information Extraction Based on Hyperspectral Remote Sensing Imagery. *Remote Sens.* **2017**, *9*, 550. [CrossRef]
90. Zhao, H.; Chen, X. Use of normalized difference bareness index in quickly mapping bare areas from TM/ETM+. In Proceedings of the 2005 IEEE International Geoscience and Remote Sensing Symposium, 2005. IGARSS '05, Seoul, Korea, 29 July 2005; pp. 1666–1668.
91. Sinha, P.; Verma, N.K.; Ayele, E. Urban Built-up Area Extraction and Change Detection of Adama Municipal Area using Time-Series Landsat Images. *Int. J. Adv. Remote Sens. GIS* **2016**, *5*, 1886–1895. [CrossRef]
92. Bouhennache, R.; Bouden, T.; Taleb, A.; Chaddad, A. Extraction of urban land features from TM Landsat image using the land features index and Tasseled cap transformation. *World Acad. Sci. Eng. Technol. Int. J. Geol. Environ. Eng.* **2015**, *2*, 142–147.
93. Wang, Z.; Gang, C.; Li, X.; Chen, Y.; Li, J. Application of a normalized difference impervious index (NDII) to extract urban impervious surface features based on Landsat TM images. *Int. J. Remote Sens.* **2015**, *36*, 1055–1069. [CrossRef]
94. Xu, H. Analysis of impervious surface and its impact on urban heat environment using the normalized difference impervious surface index (NDISI). *Photogramm. Eng. Remote Sens.* **2010**, *76*, 557–565. [CrossRef]
95. Yang, J.; He, Y.; Caspersen, J. Fully constrained linear spectral unmixing based global shadow compensation for high resolution satellite imagery of urban areas. *Int. J. Appl. Earth Obs.* **2015**, *38*, 88–98. [CrossRef]
96. De Roeck, T.; Van de Voorde, T.; Canters, F. Full hierarchic versus non-hierarchic classification approaches for mapping sealed surfaces at the rural-urban fringe using high-resolution satellite data. *Sensors* **2009**, *9*, 22–45. [CrossRef]
97. Seneviratne, S.I.; Corti, T.; Davin, E.L.; Hirschi, M.; Jaeger, E.B.; Lehner, I.; Orlowsky, B.; Teuling, A.J. Investigating soil moisture–climate interactions in a changing climate: A review. *Earth-Sci. Rev.* **2010**, *99*, 125–161. [CrossRef]
98. Pangaluru, K.; Velicogna, I.; Mohajerani, Y.; Ciracì, E.; Cpepa, S.; Basha, G.; Rao, S. Soil Moisture Variability in India: Relationship of Land Surface–Atmosphere Fields Using Maximum Covariance Analysis. *Remote Sens.* **2019**, *11*, 335. [CrossRef]
99. Bao, Y.; Lin, L.; Wu, S.; Deng, K.A.K.; Petropoulos, G.P. Surface soil moisture retrievals over partially vegetated areas from the synergy of Sentinel-1 and Landsat 8 data using a modified water-cloud model. *Int. J. Appl. Earth Obs.* **2018**, *72*, 76–85. [CrossRef]
100. Veroustraete, F.; Li, Q.; Verstraeten, W.W.; Chen, X.; Bao, A.; Dong, Q.; Liu, T.; Willems, P. Soil moisture content retrieval based on apparent thermal inertia for Xinjiang province in China. *Int. J. Remote Sens.* **2012**, *33*, 3870–3885. [CrossRef]
101. Friedl, M. Forward and inverse modeling of land surface energy balance using surface temperature measurements. *Remote Sens. Envuron.* **2002**, *79*, 344–354. [CrossRef]
102. Firozjaei, M.K.; Kiavarz, M.; Nematollahi, O.; Karimpour Reihan, M.; Alavipanah, S.K. An evaluation of energy balance parameters, and the relations between topographical and biophysical characteristics using the mountainous surface energy balance algorithm for land (SEBAL). *Int. J. Remote Sens.* **2019**, *40*, 5230–5260. [CrossRef]
103. Firozjaei, M.K.; Weng, Q.; Zhao, C.; Kiavarz, M.; Lu, L.; Alavipanah, S.K. Surface anthropogenic heat islands in six megacities: An assessment based on a triple-source surface energy balance model. *Remote Sens. Environ.* **2020**, *242*, 111751. [CrossRef]

104. Weng, Q.; Firozjaei, M.K.; Kiavarz, M.; Alavipanah, S.K.; Hamzeh, S. Normalizing land surface temperature for environmental parameters in mountainous and urban areas of a cold semi-arid climate. *Sci. Total Environ.* **2019**, *650*, 515–529. [CrossRef]
105. Wan, Z.; Wang, P.; Li, X. Using MODIS land surface temperature and normalized difference vegetation index products for monitoring drought in the southern Great Plains, USA. *Int. J. Remote Sens.* **2004**, *25*, 61–72. [CrossRef]
106. Ma, J.; Chen, S.; Hu, X.; Liu, P.; Liu, L. Spatial-temporal variation of the land surface temperature field and present-day tectonic activity. *Geosci. Front.* **2010**, *1*, 57–67. [CrossRef]
107. Firozjaei, M.K.; Kiavarz, M.; Alavipanah, S.K.; Lakes, T.; Qureshi, S. Monitoring and forecasting heat island intensity through multi-temporal image analysis and cellular automata-Markov chain modelling: A case of Babol city, Iran. *Ecol. Indic.* **2018**, *91*, 155–170. [CrossRef]
108. Alavipanah, S.K.; Kiavarz, M.; Firozjaei, M.K. Monitoring spatiotemporal changes of heat island in babol city due to land use changes. *Int. Arch. Photogramm. Remote Sens. Spat. Inf. Sci.* **2017**, *42*, 17–22. [CrossRef]
109. Firozjaei, M.K.; Fathololoumi, S.; Mijani, N.; Kiavarz, M.; Qureshi, S.; Homaee, M.; Alavipanah, S.K. Evaluating the spectral indices efficiency to quantify daytime surface anthropogenic heat island intensity: An intercontinental methodology. *Remote Sens.* **2020**, *12*, 2854. [CrossRef]
110. Shorabeh, S.N.; Kakroodi, A.A.; Firozjaei, M.K.; Minaei, F.; Homaee, M. Impact Assessment Modeling of Climatic Conditions on Spatial-temporal Changes in Surface Biophysical Properties Driven by Urban Physical Expansion Using Satellite Images. *Sustain. Cities Soc.* **2022**, *80*, 103757. [CrossRef]
111. Mijani, N.; Alavipanah, S.K.; Firozjaei, M.K.; Arsanjani, J.J.; Hamzeh, S.; Weng, Q. Modeling outdoor thermal comfort using satellite imagery: A principle component analysis-based approach. *Ecol. Indic.* **2020**, *117*, 106555. [CrossRef]
112. Harris, P.P.; Folwell, S.S.; Gallego-Elvira, B.; Rodríguez, J.; Milton, S.; Taylor, C.M. An evaluation of modeled evaporation regimes in Europe using observed dry spell land surface temperature. *J. Hydrometeorol.* **2017**, *18*, 1453–1470. [CrossRef]
113. Jia, L.; Marco, M.; Bob, S.; Lu, J.; Massimo, M. Monitoring Water Resources and Water Use from Earth Observation in the Belt and Road Countries. *Bull. Chin. Acad. Sci.* **2017**, *32*, 62–73.
114. Lievens, H.; Martens, B.; Verhoest, N.; Hahn, S.; Reichle, R.; Miralles, D. Assimilation of global radar backscatter and radiometer brightness temperature observations to improve soil moisture and land evaporation estimates. *Remote Sens. Environ.* **2017**, *189*, 194–210. [CrossRef]
115. Fathololoumi, S.; Vaezi, A.R.; Firozjaei, M.K.; Biswas, A. Quantifying the effect of surface heterogeneity on soil moisture across regions and surface characteristic. *J. Hydrol.* **2021**, *596*, 126132. [CrossRef]
116. Pinheiro, A.C.; Privette, J.L.; Mahoney, R.; Tucker, C.J. Directional effects in a daily AVHRR land surface temperature dataset over Africa. *IEEE Trans. Geosci. Remote Sens.* **2004**, *42*, 1941–1954. [CrossRef]
117. Ermida, S.L.; DaCamara, C.C.; Trigo, I.F.; Pires, A.C.; Ghent, D.; Remedios, J. Modelling directional effects on remotely sensed land surface temperature. *Remote Sens. Environ.* **2017**, *190*, 56–69. [CrossRef]
118. Aboutalebi, M.; Torres-Rua, A.F.; McKee, M.; Nieto, H.; Kustas, W.; Coopmans, C. The impact of shadows on partitioning of radiometric temperature to canopy and soil temperature based on the contextual two-source energy balance model (TSEB-2T). In Proceedings of the Autonomous Air and Ground Sensing Systems for Agricultural Optimization and Phenotyping IV, Baltimore, ML, USA, 15–16 April 2019; p. 1100804.
119. Ermida, S.L.; Trigo, I.F.; DaCamara, C.C.; Göttsche, F.M.; Olesen, F.S.; Hulley, G. Validation of remotely sensed surface temperature over an oak woodland landscape—The problem of viewing and illumination geometries. *Remote Sens. Environ.* **2014**, *148*, 16–27. [CrossRef]
120. Yuge, K.; Itou, M.; Nakano, Y.; Kuroda, M.; Haraguchi, T. Soil Moisture and Temperature Changes Affected by an Isolated Plant Shadow. *J. Agric. Meteorol.* **2005**, *60*, 717–720. [CrossRef]
121. Barroso, C.; Trigo, I.; Olesen, F.; DaCamara, C.; Queluz, M. Intercalibration of NOAA and Meteosat window channel brightness temperatures. *Int. J. Remote Sens.* **2005**, *26*, 3717–3733. [CrossRef]
122. Jiao, Z.-H.; Yan, G.; Wang, T.; Mu, X.; Zhao, J. Modeling of Land Surface Thermal Anisotropy Based on Directional and Equivalent Brightness Temperatures Over Complex Terrain. *IEEE J. Sel. Top. Appl. Earth Obs. Remote Sens.* **2019**, *12*, 410–423. [CrossRef]
123. Kato, S.; Matsunaga, T.; Yamaguchi, Y. Influence of shade on surface temperature in an urban area estimated by ASTER data. *Int. Arch. Photogammetry Remote Sens. Spat. Inf. Sci. Kyoto Jpn.* **2010**, *38*, 925–929.
124. Li, J.; Song, C.; Cao, L.; Zhu, F.; Meng, X.; Wu, J. Impacts of landscape structure on surface urban heat islands: A case study of Shanghai, China. *Remote Sens. Environ.* **2011**, *115*, 3249–3263. [CrossRef]
125. Hertel, D.; Schlink, U. Decomposition of urban temperatures for targeted climate change adaptation. *Environ. Model. Softw.* **2019**, *113*, 20–28. [CrossRef]
126. Mathew, A.; Khandelwal, S.; Kaul, N. Investigating spatial and seasonal variations of urban heat island effect over Jaipur city and its relationship with vegetation, urbanization and elevation parameters. *Sustain. Cities Soc.* **2017**, *35*, 157–177. [CrossRef]
127. Martinelli, L.; Lin, T.-P.; Matzarakis, A. Assessment of the influence of daily shadings pattern on human thermal comfort and attendance in Rome during summer period. *Build. Environ.* **2015**, *92*, 30–38. [CrossRef]
128. Yu, K.; Chen, Y.; Wang, D.; Chen, Z.; Gong, A.; Li, J. Study of the Seasonal Effect of Building Shadows on Urban Land Surface Temperatures Based on Remote Sensing Data. *Remote Sens.* **2019**, *11*, 497. [CrossRef]
129. Zhao, L.; Lee, X.; Smith, R.B.; Oleson, K. Strong contributions of local background climate to urban heat islands. *Nature* **2014**, *511*, 216. [CrossRef] [PubMed]

130. Li, X.; Strahler, A.H. Geometric-optical modeling of a conifer forest canopy. *IEEE Trans. Geosci. Remote Sens.* **1985**, *5*, 705–721. [CrossRef]
131. Ono, A.; Kajiwara, K.; Honda, Y. Development of new vegetation indexes, shadow index (SI) and water stress trend (WST). *Intern. Arch. Photogramm. Remote Sens. Spat. Inf. Sci.* **2010**, *38*, 710–714.
132. Liu, X.; Hou, Z.; Shi, Z.; Bo, Y.; Cheng, J. A shadow identification method using vegetation indices derived from hyperspectral data. *Int. J. Remote Sens.* **2017**, *38*, 5357–5373. [CrossRef]
133. Huemmrich, K.F. Effects of shadows on vegetation indices. In Proceedings of the IGARSS '96. 1996 International Geoscience and Remote Sensing Symposium, 'Remote Sensing for a Sustainable Future', Lincoln, NE, USA, 31 May 1996; pp. 2372–2374.
134. Wang, J.; Wang, B.; Liu, Y.; Huang, H. Analysis of Slope and NDVI Effects on Land Surface Temperature Retrieval Accuracy in Mountain Area Based on WIS Data of Tiangong-2. In Proceedings of the Tiangong-2 Remote Sensing Application Conference; Springer: Berlin/Heidelberg, Germany, 2019; pp. 180–191.
135. He, T.; Gao, F.; Liang, S.; Peng, Y. Mapping Climatological Bare Soil Albedos over the Contiguous United States Using MODIS Data. *Remote Sens.* **2019**, *11*, 666. [CrossRef]
136. Pettorelli, N.; Vik, J.O.; Mysterud, A.; Gaillard, J.-M.; Tucker, C.J.; Stenseth, N.C. Using the satellite-derived NDVI to assess ecological responses to environmental change. *Trends Ecol. Evol.* **2005**, *20*, 503–510. [CrossRef]
137. Gonzalez-Dugo, V.; Zarco-Tejada, P.; Berni, J.A.; Suárez, L.; Goldhamer, D.; Fereres, E. Almond tree canopy temperature reveals intra-crown variability that is water stress-dependent. *Agric. For. Meteorol.* **2012**, *154*, 156–165. [CrossRef]
138. Zarco-Tejada, P.J.; González-Dugo, V.; Williams, L.; Suárez, L.; Berni, J.A.; Goldhamer, D.; Fereres, E. A PRI-based water stress index combining structural and chlorophyll effects: Assessment using diurnal narrow-band airborne imagery and the CWSI thermal index. *Remote Sens. Environ.* **2013**, *138*, 38–50. [CrossRef]
139. Montanari, A.; Sideris, M.G. Satellite Remote Sensing of Hydrological Change. *Glob. Chang. Future Earth Geosci. Perspect.* **2018**, *3*, 57.
140. Pipitone, C.; Maltese, A.; Dardanelli, G.; Lo Brutto, M.; La Loggia, G. Monitoring water surface and level of a reservoir using different remote sensing approaches and comparison with dam displacements evaluated via GNSS. *Remote Sens.* **2018**, *10*, 71. [CrossRef]
141. Maltese, A.; Pipitone, C.; Dardanelli, G.; Capodici, F.; Muller, J.-P. Toward a comprehensive dam monitoring: On-site and remote-retrieved forcing factors and resulting displacements (GNSS and PS–InSAR). *Remote Sens.* **2021**, *13*, 1543. [CrossRef]
142. Ma, Y.; Xu, N.; Sun, J.; Wang, X.H.; Yang, F.; Li, S. Estimating water levels and volumes of lakes dated back to the 1980s using Landsat imagery and photon-counting lidar datasets. *Remote Sens. Environ.* **2019**, *232*, 111287. [CrossRef]
143. Xu, H. Modification of normalised difference water index (NDWI) to enhance open water features in remotely sensed imagery. *Int. J. Remote Sens.* **2006**, *27*, 3025–3033. [CrossRef]
144. Li, L.; Yan, Z.; Shen, Q.; Cheng, G.; Gao, L.; Zhang, B. Water Body Extraction from Very High Spatial Resolution Remote Sensing Data Based on Fully Convolutional Networks. *Remote Sens.* **2019**, *11*, 1162. [CrossRef]
145. Feyisa, G.L.; Meilby, H.; Fensholt, R.; Proud, S.R. Automated Water Extraction Index: A new technique for surface water mapping using Landsat imagery. *Remote Sens. Environ.* **2014**, *140*, 23–35. [CrossRef]
146. Rundquist, D.C.; Lawson, M.P.; Queen, L.P.; Cerveny, R.S. The relationship between summer-season rainfall events and lake-surface area. *JAWRA J. Am. Water Resour. Assoc.* **1987**, *23*, 493–508. [CrossRef]
147. Xie, H.; Luo, X.; Xu, X.; Tong, X.; Jin, Y.; Pan, H.; Zhou, B. New hyperspectral difference water index for the extraction of urban water bodies by the use of airborne hyperspectral images. *J. Appl. Remote Sens.* **2014**, *8*, 085098. [CrossRef]
148. Moradi, M.; Sahebi, M.; Shokri, M. Modified optimization water index (mowi) for landsat-8 oli/tirs. *ISPRS-Int. Arch. Photogramm. Remote Sens. Spat. Inf. Sci.* **2017**, *42*, 185–190. [CrossRef]
149. Adeline, K.; Chen, M.; Briottet, X.; Pang, S.; Paparoditis, N. Shadow detection in very high spatial resolution aerial images: A comparative study. *ISPRS J. Photogramm. Remote Sens.* **2013**, *80*, 21–38. [CrossRef]
150. Movia, A.; Beinat, A.; Crosilla, F. Shadow detection and removal in RGB VHR images for land use unsupervised classification. *ISPRS J. Photogramm. Remote Sens.* **2016**, *119*, 485–495. [CrossRef]
151. Firozjaei, M.K.; Daryaei, I.; Sedighi, A.; Weng, Q.; Alavipanah, S.K. Homogeneity Distance Classification Algorithm (HDCA): A Novel Algorithm for Satellite Image Classification. *Remote Sens.* **2019**, *11*, 546. [CrossRef]
152. Firozjaei, M.K.; Sedighi, A.; Kiavarz, M.; Qureshi, S.; Haase, D.; Alavipanah, S.K. Automated Built-Up Extraction Index: A New Technique for Mapping Surface Built-Up Areas Using LANDSAT 8 OLI Imagery. *Remote Sens.* **2019**, *11*, 1966. [CrossRef]
153. Lu, D.; Hetrick, S.; Moran, E. Land cover classification in a complex urban-rural landscape with QuickBird imagery. *Photogramm. Eng. Remote Sens.* **2010**, *76*, 1159–1168. [CrossRef]
154. Lopatin, J.; Dolos, K.; Kattenborn, T.; Fassnacht, F.E. How canopy shadow affects invasive plant species classification in high spatial resolution remote sensing. *Remote Sens. Ecol. Conserv.* **2019**, *5*, 302–317. [CrossRef]
155. Mogare, S. A Survey on Various Shadow Detection and Removal Methods/Algorithms. *Int. J. Recent Trends Eng. Res.* **2016**, *2*, 262–266.
156. Arévalo, V.; González, J.; Ambrosio, G. Shadow detection in colour high-resolution satellite images. *Int. J. Remote Sens.* **2008**, *29*, 1945–1963. [CrossRef]

157. Aboutalebi, M.; Torres-Rua, A.F.; Kustas, W.P.; Nieto, H.; Coopmans, C.; McKee, M. Assessment of different methods for shadow detection in high-resolution optical imagery and evaluation of shadow impact on calculation of NDVI, and evapotranspiration. *Irrig. Sci.* **2019**, *37*, 407–429. [CrossRef]
158. Qiu, S.; He, B.; Zhu, Z.; Liao, Z.; Quan, X. Improving Fmask cloud and cloud shadow detection in mountainous area for Landsats 4–8 images. *Remote Sens. Environ.* **2017**, *199*, 107–119. [CrossRef]
159. Zhang, H.; Sun, K.; Li, W. Object-oriented shadow detection and removal from urban high-resolution remote sensing images. *IEEE Trans. Geosci. Remote Sens.* **2014**, *52*, 6972–6982. [CrossRef]
160. Mostafa, Y.; Abdelhafiz, A. Accurate shadow detection from high-resolution satellite images. *IEEE Geosci. Remote Sens. Lett.* **2017**, *14*, 494–498. [CrossRef]
161. Martinuzzi, S.; Gould, W.A.; González, O.M.R. *Creating Cloud-Free Landsat ETM+ Data Sets in Tropical Landscapes: Cloud and Cloud-Shadow Removal*; Gen. Tech. Rep. IITF-32; U.S. Department of Agriculture, Forest Service, International Institute of Tropical Forestry: Washington, DC, USA, 2007.
162. Dare, P.M. Shadow analysis in high-resolution satellite imagery of urban areas. *Photogramm. Eng. Remote Sens.* **2005**, *71*, 169–177. [CrossRef]
163. Polidorio, A.M.; Flores, F.C.; Imai, N.N.; Tommaselli, A.M.; Franco, C. Automatic shadow segmentation in aerial color images. In Proceedings of the 16th Brazilian Symposium on Computer Graphics and Image Processing (SIBGRAPI 2003), Sao Carlos, Brazil, 12–15 October 2003; pp. 270–277.
164. Nagao, M.; Matsuyama, T.; Ikeda, Y. Region extraction and shape analysis in aerial photographs. *Comput. Graph. Image Process.* **1979**, *10*, 195–223. [CrossRef]
165. Otsu, N. A threshold selection method from gray-level histograms. *IEEE Trans. Syst. Man Cybern.* **1979**, *9*, 62–66. [CrossRef]
166. Yamazaki, F.; Liu, W.; Takasaki, M. Characteristics of shadow and removal of its effects for remote sensing imagery. In Proceedings of the 2009 IEEE International Geoscience and Remote Sensing Symposium, Cape Town, South Africa, 12–17 July 2009; pp. IV-426–IV-429.
167. Wang, T.; Li, Y.; Yu, S.; Liu, Y. Estimating the Volume of Oil Tanks Based on High-Resolution Remote Sensing Images. *Remote Sens.* **2019**, *11*, 793. [CrossRef]
168. Ghandour, A.J.; Jezzini, A.A. Building shadow detection based on multi-thresholding segmentation. *Signal Image Video Process.* **2019**, *13*, 349–357. [CrossRef]
169. Greeshma, N.; Baburaj, M.; George, S.N. Reconstruction of cloud-contaminated satellite remote sensing images using kernel pca-based image modelling. *Arab. J. Geosci.* **2016**, *9*, 239.
170. Zhai, H.; Zhang, H.; Zhang, L.; Li, P. Cloud/shadow detection based on spectral indices for multi/hyperspectral optical remote sensing imagery. *ISPRS J. Photogramm. Remote Sens.* **2018**, *144*, 235–253. [CrossRef]
171. Gao, J.; Li, J.; Li, Y. Approximate event detection over multi-modal sensing data. *J. Comb. Optim.* **2016**, *32*, 1002–1016. [CrossRef]
172. Chen, M.; Zhuang, Q.; He, Y. An efficient method of estimating downward solar radiation based on the MODIS observations for the use of land surface modeling. *Remote Sens.* **2014**, *6*, 7136–7157. [CrossRef]
173. Volkovs, M.N.; Zemel, R.S. New learning methods for supervised and unsupervised preference aggregation. *J. Mach. Learn. Res.* **2014**, *15*, 1135–1176.
174. Han, H.; Han, C.; Lan, T.; Huang, L.; Hu, C.; Xue, X. Automatic shadow detection for multispectral satellite remote sensing images in invariant color spaces. *Appl. Sci.* **2020**, *10*, 6467. [CrossRef]
175. Luo, S.; Li, H.; Shen, H. Deeply supervised convolutional neural network for shadow detection based on a novel aerial shadow imagery dataset. *ISPRS J. Photogramm. Remote Sens.* **2020**, *167*, 443–457. [CrossRef]
176. Ok, A.O. Automated detection of buildings from single VHR multispectral images using shadow information and graph cuts. *ISPRS J. Photogramm. Remote Sens.* **2013**, *86*, 21–40. [CrossRef]
177. Zigh, E.; Kouninef, B.; Kadiri, M. Removing shadows using RGB color space in pairs of optical satellite images. *J. Indian Soc. Remote Sens.* **2017**, *45*, 431–441. [CrossRef]
178. Jia, K.; Li, Q.; Wei, X.; Zhang, L.; Du, X.; Yao, Y.; Wang, X. Multi-temporal remote sensing data applied in automatic land cover update using iterative training sample selection and Markov Random Field model. *Geocarto Int.* **2015**, *30*, 882–893. [CrossRef]
179. Xie, F.; Shi, M.; Shi, Z.; Yin, J.; Zhao, D. Multilevel cloud detection in remote sensing images based on deep learning. *IEEE J. Sel. Top. Appl. Earth Obs. Remote Sens.* **2017**, *10*, 3631–3640. [CrossRef]
180. Zi, Y.; Xie, F.; Jiang, Z. A cloud detection method for Landsat 8 images based on PCANet. *Remote Sens.* **2018**, *10*, 877. [CrossRef]
181. Li, Z.; Shen, H.; Cheng, Q.; Liu, Y.; You, S.; He, Z. Deep learning based cloud detection for medium and high resolution remote sensing images of different sensors. *ISPRS J. Photogramm. Remote Sens.* **2019**, *150*, 197–212. [CrossRef]
182. Li, Z.; Shen, H.; Wei, Y.; Cheng, Q.; Yuan, Q. Cloud detection by fusing multi-scale convolutional features. *Proc. ISPRS Ann. Photogramm. Remote Sens. Spat. Inf. Sci.* **2018**, *4*, 149–152. [CrossRef]
183. Chai, D.; Newsam, S.; Zhang, H.K.; Qiu, Y.; Huang, J. Cloud and cloud shadow detection in Landsat imagery based on deep convolutional neural networks. *Remote Sens. Environ.* **2019**, *225*, 307–316. [CrossRef]
184. Khan, S.H.; Bennamoun, M.; Sohel, F.; Togneri, R. Automatic shadow detection and removal from a single image. *IEEE Trans. Pattern Anal. Mach. Intell.* **2015**, *38*, 431–446. [CrossRef]
185. Yin, S.; Liu, J.; Li, H. A self-supervised learning method for shadow detection in remote sensing imagery. *3D Res.* **2018**, *9*, 51. [CrossRef]

186. Deng, C.; Wu, C. BCI: A biophysical composition index for remote sensing of urban environments. *Remote Sens. Environ.* **2012**, *127*, 247–259. [CrossRef]
187. Sun, L.; Liu, X.; Yang, Y.; Chen, T.; Wang, Q.; Zhou, X. A cloud shadow detection method combined with cloud height iteration and spectral analysis for Landsat 8 OLI data. *ISPRS J. Photogramm. Remote Sens.* **2018**, *138*, 193–207. [CrossRef]
188. Hsieh, Y.-T.; Wu, S.-T.; Chen, C.-T.; Chen, J.-C. Analyzing spectral characteristics of shadow area from ads-40 high radiometric resolution aerial images. *Int. Arch. Photogramm. Remote Sens. Spat. Inf. Sci.* **2016**, *41*, 223–227. [CrossRef]
189. Sarabandi, P.; Yamazaki, F.; Matsuoka, M.; Kiremidjian, A. Shadow detection and radiometric restoration in satellite high resolution images. In Proceedings of the IGARSS 2004. 2004 IEEE International Geoscience and Remote Sensing Symposium, Anchorage, AK, USA, 20–24 September 2004; pp. 3744–3747.
190. Jin, S.; Homer, C.; Yang, L.; Xian, G.; Fry, J.; Danielson, P.; Townsend, P.A. Automated cloud and shadow detection and filling using two-date Landsat imagery in the USA. *Int. J. Remote Sens.* **2013**, *34*, 1540–1560. [CrossRef]
191. Wang, B.; Ono, A.; Muramatsu, K.; Fujiwara, N. Automated detection and removal of clouds and their shadows from Landsat TM images. *IEICE Trans. Inf. Syst.* **1999**, *82*, 453–460.
192. Zhu, X.; Helmer, E.H. An automatic method for screening clouds and cloud shadows in optical satellite image time series in cloudy regions. *Remote Sens. Environ.* **2018**, *214*, 135–153. [CrossRef]
193. Du, W.; Qin, Z.; Fan, J.; Gao, M.; Wang, F.; Abbasi, B. An Efficient Approach to Remove Thick Cloud in VNIR Bands of Multi-Temporal Remote Sensing Images. *Remote Sens.* **2019**, *11*, 1284. [CrossRef]
194. Deutsch, A.N.; Chabot, N.L.; Mazarico, E.; Ernst, C.M.; Head, J.W.; Neumann, G.A.; Solomon, S.C. Comparison of areas in shadow from imaging and altimetry in the north polar region of Mercury and implications for polar ice deposits. *Icarus* **2016**, *280*, 158–171. [CrossRef] [PubMed]
195. Lu, D. Detection and substitution of clouds/hazes and their cast shadows on IKONOS images. *Int. J. Remote Sens.* **2007**, *28*, 4027–4035. [CrossRef]
196. Wen, Z.; Shao, G.; Mirza, Z.A.; Chen, J.; Lü, M.; Wu, S. Restoration of shadows in multispectral imagery using surface reflectance relationships with nearby similar areas. *Int. J. Remote Sens.* **2015**, *36*, 4195–4212. [CrossRef]
197. Wan, C.-Y.; King, B.A.; Li, Z. An assessment of shadow enhanced urban remote sensing imagery of a complex city-Hong Kong. *Int. Arch. Photogramm. Remote Sens. Spat. Inf. Sci.* **2012**, *39*, 177–182. [CrossRef]
198. Wang, Q.J.; Tian, Q.J.; Lin, Q.Z.; Li, M.X.; Wang, L.M. An improved algorithm for shadow restoration of high spatial resolution imagery. In Proceedings of the Remote Sensing of the Environment: 16th National Symposium on Remote Sensing of China, Beijing, China, 7–10 September 2007; p. 71230D.
199. Kouchi, K.I.; Yamazaki, F. Characteristics of tsunami-affected areas in moderate-resolution satellite images. *IEEE Trans. Geosci. Remote Sens.* **2007**, *45*, 1650–1657. [CrossRef]
200. Massalabi, A.; He, D.-C.; Benie, G.B.; Beaudry, E. Detecting information under and from shadow in panchromatic Ikonos images of the city of Sherbrooke. In Proceedings of the IGARSS 2004. 2004 IEEE International Geoscience and Remote Sensing Symposium, Anchorage, AK, USA, 20–24 September 2004; pp. 2000–2003.
201. Rau, J.; Chen, N.-Y.; Chen, L.-C. True orthophoto generation of built-up areas using multi-view images. *Photogramm. Eng. Remote Sens.* **2002**, *68*, 581–588.
202. Tseng, D.-C.; Tseng, H.-T.; Chien, C.-L. Automatic cloud removal from multi-temporal SPOT images. *Appl. Math. Comput.* **2008**, *205*, 584–600. [CrossRef]
203. Goetz, S.J.; Wright, R.K.; Smith, A.J.; Zinecker, E.; Schaub, E. IKONOS imagery for resource management: Tree cover, impervious surfaces, and riparian buffer analyses in the mid-Atlantic region. *Remote Sens. Environ.* **2003**, *88*, 195–208. [CrossRef]
204. Giles, P.T. Remote sensing and cast shadows in mountainous terrain. *Photogramm. Eng. Remote Sens.* **2001**, *67*, 833–840.
205. Jiang, H.; Wang, S.; Cao, X.; Yang, C.; Zhang, Z.; Wang, X. A shadow-eliminated vegetation index (SEVI) for removal of self and cast shadow effects on vegetation in rugged terrains. *Int. J. Digit. Earth* **2019**, *12*, 1013–1029. [CrossRef]
206. Gao, Y.; Zhang, W. A simple empirical topographic correction method for ETM+ imagery. *Int. J. Remote Sens.* **2009**, *30*, 2259–2275. [CrossRef]
207. Proy, C.; Tanre, D.; Deschamps, P. Evaluation of topographic effects in remotely sensed data. *Remote Sens. Environ.* **1989**, *30*, 21–32. [CrossRef]
208. Conese, C. Topographic normalization of TM scenes through the use of an atmospheric correction method and digital terrain model. *Photogramm. Eng. Remote Sens.* **1993**, *59*, 1745–1753.
209. Vanonckelen, S.; Lhermitte, S.; Van Rompaey, A. The effect of atmospheric and topographic correction methods on land cover classification accuracy. *Int. J. Appl. Earth Obs. Geoinf.* **2013**, *24*, 9–21. [CrossRef]
210. Moreira, E.P.; Valeriano, M.M. Application and evaluation of topographic correction methods to improve land cover mapping using object-based classification. *Int. J. Appl. Earth Obs. Geoinf.* **2014**, *32*, 208–217. [CrossRef]
211. Smith, J.; Lin, T.L.; Ranson, K. The Lambertian assumption and Landsat data. *Photogramm. Eng. Remote Sens.* **1980**, *46*, 1183–1189.
212. Minnaert, M. The reciprocity principle in lunar photometry. *Astrophys. J.* **1941**, *93*, 403–410. [CrossRef]
213. Ekstrand, S. Landsat TM-based forest damage assessment: Correction for topographic effects. *Photogramm. Eng. Remote Sens.* **1996**, *62*, 151–162.
214. Meyer, P.; Itten, K.I.; Kellenberger, T.; Sandmeier, S.; Sandmeier, R. Radiometric corrections of topographically induced effects on Landsat TM data in an alpine environment. *ISPRS J. Photogramm. Remote Sens.* **1993**, *48*, 17–28. [CrossRef]

215. Gu, D.; Gillespie, A. Topographic normalization of Landsat TM images of forest based on subpixel sun–canopy–sensor geometry. *Remote Sens. Environ.* **1998**, *64*, 166–175. [CrossRef]
216. Soenen, S.; Peddle, D.; Coburn, C.; Hall, R.; Hall, F. Improved topographic correction of forest image data using a 3-D canopy reflectance model in multiple forward mode. *Int. J. Remote Sens.* **2008**, *29*, 1007–1027. [CrossRef]
217. Wang, Q.; Yan, L. Anisotropic scattering shadow compensation method for remote sensing image with consideration of terrain. *Int. Arch. Photogramm. Remote Sens. Spat. Inf. Sci.* **2016**, *41*, 401–405. [CrossRef]
218. Li, H.; Xu, L.; Shen, H.; Zhang, L. A general variational framework considering cast shadows for the topographic correction of remote sensing imagery. *ISPRS J. Photogramm. Remote Sens.* **2016**, *117*, 161–171. [CrossRef]
219. Xia, M.; Wang, T.; Zhang, Y.; Liu, J.; Xu, Y. Cloud/shadow segmentation based on global attention feature fusion residual network for remote sensing imagery. *Int. J. Remote Sens.* **2021**, *42*, 2022–2045. [CrossRef]
220. Miao, S.; Xia, M.; Qian, M.; Zhang, Y.; Liu, J.; Lin, H. Cloud/shadow segmentation based on multi-level feature enhanced network for remote sensing imagery. *Int. J. Remote Sens.* **2022**, *44*, 1–21. [CrossRef]
221. Zhang, C.; Li, W.; Travis, D.J. Restoration of clouded pixels in multispectral remotely sensed imagery with cokriging. *Int. J. Remote Sens.* **2009**, *30*, 2173–2195. [CrossRef]
222. Song, M.; Civco, D.L. A knowledge-based approach for reducing cloud and shadow. In Proceedings of the 2002 ASPRS-ACSM Annual Conferenceand FIG XXII Congress, Washington, DC, USA, 22–26 April 2002; pp. 22–26.
223. Leblon, B.; Gallant, L.; Granberg, H. Effects of shadowing types on ground-measured visible and near-infrared shadow reflectances. *Remote Sens. Environ.* **1996**, *58*, 322–328. [CrossRef]
224. Lu, D.; Weng, Q. A survey of image classification methods and techniques for improving classification performance. *Int. J. Remote Sens.* **2007**, *28*, 823–870. [CrossRef]
225. Matsushita, B.; Yang, W.; Chen, J.; Onda, Y.; Qiu, G. Sensitivity of the enhanced vegetation index (EVI) and normalized difference vegetation index (NDVI) to topographic effects: A case study in high-density cypress forest. *Sensors* **2007**, *7*, 2636–2651. [CrossRef]